

# Sub-picosecond thermalization dynamics in condensation of strongly coupled lattice plasmons

Aaro I. Väkeväinen,<sup>1</sup> Antti J. Moilanen,<sup>1</sup> Marek Nečada,<sup>1</sup>  
Tommi K. Hakala,<sup>2</sup> Konstantinos S. Daskalakis,<sup>1</sup> Päivi Törmä<sup>1\*</sup>

<sup>1</sup>Department of Applied Physics, Aalto University School of Science,  
P.O. Box 15100, Aalto, FI-00076, Finland

<sup>2</sup>Institute of Photonics, University of Eastern Finland,  
P.O. Box 111, Joensuu, FI-80101, Finland

\*To whom correspondence should be addressed; E-mail: paivi.torma@aalto.fi.

**Bosonic condensates offer exciting prospects for studies of non-equilibrium quantum dynamics. Understanding the dynamics is particularly challenging in the sub-picosecond timescales typical for room temperature luminous driven-dissipative condensates. Here we combine a lattice of plasmonic nanoparticles with dye molecule solution at the strong coupling regime, and pump the molecules optically. The emitted light reveals three distinct regimes: one-dimensional lasing, stimulated thermalization, and two-dimensional multimode condensation. The condensate is achieved by matching the thermalization rate with the lattice size and occurs only for pump pulse durations below a critical value. Our results give a direct access to spatiotemporal control and monitoring of thermalization processes and condensate formation at sub-picosecond timescales.**

# Introduction

Ideal Bose-Einstein condensation means accumulation of macroscopic population to a single ground state in an equilibrium system, with emergence of long-range order. Bosonic condensation in non- or quasi-equilibrium and driven-dissipative systems extends this concept and offers plentiful new phenomena, such as loss of algebraically decaying phase order (1, 2), generalized Bose-Einstein condensation (BEC) into multiple states (3), rich phase diagrams of lasing, condensation and superradiance phenomena (4, 5), and quantum simulation of the XY model that is at the heart of many optimization problems (6). Such condensates may also be a powerful system to explore dynamical quantum phase transitions (7). Each presently available condensate system offers different advantages and limitations concerning studies of non- and quasi-equilibrium dynamics. The ability to tune interactions precisely over a wide range is the major advantage of ultracold gases (8, 9). Polariton condensates (10–18) offer high critical temperatures compared to ultracold gases. In photon condensates (19, 20), the thermal bath is easily controlled (21, 22). Recently periodic two-dimensional (2D) arrays of metal nanoparticles, so-called plasmonic lattices or crystals (23), have emerged as a multifaceted platform for room temperature lasing and condensation at weak (24–28) and strong coupling (29, 30) regimes.

In plasmonic lattices, the lattice geometry and periodicity, the size and shape of the nanoparticles, and the overall size of the lattice can be controlled with nanometer accuracy and independent of one another. The energy where condensation or lasing occurs is given by the band edge energy that depends on the period of the array. Remarkably the band edge energy and the dispersion are extremely constant over large lattices (accuracy 0.1% (28)). In semiconductor polariton condensates, disorder in the samples often leads to traps and fragmentation (15), or condensates may be trapped by geometry (16, 19). Thus plasmonic lattices offer a feature complementary to other condensate systems, namely that propagation of excitations over the lattice can be used for monitoring time-evolution of such processes as thermalization: each position in the array can be related to time via the group velocity, and there are no spurious effects due to non-uniformity of the sample. Spatially resolved luminescence was utilized in this way in the first observation of a BEC in a plasmonic lattice (28).

Here we show that formation of a condensate with a pronounced thermal distribution is pos-

sible at a 200 fs timescale and attribute this strikingly fast thermalization to partially coherent dynamics due to stimulated processes and strong coupling. We observe a unique double threshold phenomenon where one-dimensional (1D) lasing occurs for lower pump fluences and two-dimensional (2D) multimode condensation, associated with thermalization, at higher fluences. The transition between lasing and condensation shown in our work is different from previous condensates (16, 28, 31–33): it relies on matching the system size, propagation of excitations, and the thermalization dynamics. Importantly we find a peculiar intermediate regime showing thermalization features but no macroscopic population at the lowest energy states. This regime allows us to reveal the stimulated nature of the thermalization process by the behavior of the luminescence in lattices of different sizes. As a direct evidence of the ultrafast character of the thermalization and condensation process, we show that it occurs only for pump pulse durations below a critical value of 100–250 fs.

## System

Our system consists of cylindrical gold nanoparticles in a rectangular lattice overlaid with a solution of organic dye molecule IR-792 (see details in Section S1). The lattice supports dispersive modes, so-called surface lattice resonances (SLRs), which are hybrid modes composed of localized surface plasmon resonances at the nanoparticles and the diffracted orders of the periodic structure (23, 34). The electric field of the SLR modes is confined to the lattice plane in which the SLR excitations can propagate. An SLR excitation can be considered a bosonic quasiparticle that consists (mostly) of a photon and of collective electron oscillation in individual metal particles. The dye molecules are pumped optically, and they can emit to the SLR modes.

We excite the sample with laser pulses at 1 kHz repetition rate and central wavelength of 800 nm, and resolve the luminescence spectrally as a function of angle and spatial position on the array, Fig. 1a (for details see Section S2). The SLR modes are classified to transverse magnetic (TM) or transverse electric (TE) depending on the polarization and propagation direction, as defined in Fig. 1b. The measured dispersions are displayed in Fig. 1c-e. In the presence of dye molecules, the SLR dispersion shifts downwards in energy with respect to the

initial diffracted order crossing. Moreover the TE modes begin to bend when approaching the molecular absorption line at 1.53 eV. These observations indicate strong coupling between the SLR and molecular excitations (35); a coupled modes fit to the data gives a Rabi splitting of 164 meV (larger than the average line width of the molecule (150 meV) and SLR (10 meV)) and an exciton part of 23% at  $k = 0$ . In the following, we refer to the hybrids of the SLR mode excitations and molecular excitons as polaritons, for brevity. To our best knowledge, this is the first time that high molecule concentration in a liquid gain solution is implemented in plasmonic lattice systems, cf. (26, 29). The plasmonic lattice, optimized for creating the condensate, has a particle diameter of 100 nm and height of 50 nm, the period in  $y$ - and  $x$ -direction of  $p_y = 570$  nm and  $p_x = 620$  nm, dye concentration of 80 mM, and a lattice size of  $100 \times 100 \mu\text{m}^2$ . The period  $p_y$  is varied between 520 and 590 nm, and the lattice size between  $40 \times 40$  and  $200 \times 200 \mu\text{m}^2$ .

## Results

We study the luminescence properties of the plasmonic lattice as a function of pump fluence, that is, the energy per unit area per excitation pulse, and find a prominent double threshold behaviour. The system is excited with an  $x$ -polarized 50 fs laser pulse that has a flat intensity profile and a size larger than the lattice. Excited polariton modes continuously leak through radiative loss, and therefore the observed luminescence intensity is directly proportional to the population of the polaritons. We record real space and momentum ( $k$ -)space intensity distributions and the corresponding spectra, the photon energy is  $E = hc/\lambda_0$  and the in-plane wave vector  $k_{x,y} = 2\pi/\lambda_0 \sin(\theta_{x,y})$ .

The sample luminescence as a function of pump fluence is presented in Fig. 2. The total luminescence intensity reveals two non-linear thresholds and a linear intermediate regime, shown in Fig. 2a. The line spectra, shown as insets, are obtained by integrating the real space spectra along the  $y$ -axis and unveil the population of polaritons as a function of energy. At the first threshold, Fig. 2b-c, lasing typical for nanoparticle arrays (24, 27, 29) is observed throughout the array. Increasing the pump fluence beyond the first threshold, Fig. 2d-e, the luminescence becomes more intense in the central part compared to the top and bottom parts of the array. Moreover luminescence at the center takes place at a lower energy than at regions closer to the

edges. We interpret this red shift as a signature of thermalizing population of polaritons that propagate along the array in  $+y$  and  $-y$  directions, discussed below. At the second threshold, Fig. 2f-g, the system undergoes a transition into a condensate: the real space intensity distribution shows uniform luminescence in the central part of the array, and the line spectrum (Fig. 2a, top inset) has a narrow peak at the band edge and a long thermalized tail at higher energies. A fit of the tail to the Maxwell–Boltzmann distribution (dashed line) gives the room temperature,  $333 \pm 12$  K (see Section S3 for more information). The spectrometer counts per emitted condensate pulse correspond to a photon number of  $\sim 10^9$  (see Section S4), which is roughly  $10^5$  times more than in the first BEC in a plasmonic lattice (28). This tremendous improvement has increased the signal-to-noise ratio so that we can now observe a prominent thermal tail (it is likely to be even longer but the data is cut due to filtering out the pump pulse). Such an upgrade of luminescence intensity is crucial for future fundamental studies and applications of this type of condensate. To produce a condensate, the periodicity must be tuned with respect to the thermalization rate and the array size (Section S5).

Three distinct regimes are also observed in the  $k$ -space intensity distributions. Fig. 3 presents the  $k$ -space images and spectra for the same sample and pump parameters as in Fig. 2. Fig. 3a-c shows that lasing spreads in the TM mode to large  $k$  (i.e., large emission angles), whereas thermalization of the polaritons occurs mostly along the TE mode, see Fig. 3d-f. At the condensation threshold, Fig. 3g-i, we observe confinement in both  $k_x$  and  $k_y$ , implying that the condensate has a 2D nature, in contrast to the lasing regime where confinement is observed only in  $k_y$ . Fig. 3j shows line spectra obtained by integrating along  $k_y$  from TE mode crosscuts (Fig. 3c,f,i); the spectrometer slit width of  $500 \mu\text{m}$  corresponds to  $\pm 1.3^\circ$  around  $\theta_x = 0$  in the 2D  $k$ -space images. Intriguingly, at the condensation threshold, we see multiple modes highly occupied at  $k_y = 0$ . The line spectrum at  $3.49 \text{ mJ/cm}^2$  shows three narrow peaks followed by a thermalized tail. The full-width at half-maximum (FWHM) of the highest peak is  $3.3 \text{ meV}$ , significantly narrower than the bare SLR mode ( $10 \text{ meV}$ ). The spacing of the multiple peaks decreases towards lower energy, ruling out the possibility of a trivial Fabry–Pérot interference. We have also observed that the spacing does not depend on the lattice size or periodicity. Based on T-matrix simulations, we attribute these modes to the finite size of the nanoparticle (Section S6). This highlights the role of the nanoparticles beyond providing a periodic structure.

Lasing and condensation transitions are expected to result in increased spatial and temporal coherence of the emitted light. Increase in temporal coherence was evidenced as the narrowing of spectral line width (Fig. 3j). To study the spatial coherence, we have performed a Michelson interferometer experiment as a function of pump fluence. In the Michelson interferometer, the real space image is split into two, one image is inverted and combined with the other one at the camera pixel array. The contrast of the observed interference fringes is extracted with a Fourier analysis of the spatial frequencies in the interfered image to exclude any artifacts produced by intensity variations in a single non-interfered image (Section S7).

In Fig. 4, the fringe contrast (proportional to the first-order correlation function  $g^{(1)}$ ) is shown as a function of pump fluence in both  $y$ - and  $x$ -directions of the lattice. High spatial coherence occurs in the  $y$ -direction over the array in both the lasing and condensation regimes (Fig. 4b-c). At the intermediate regime, the spatial coherence decreases, in agreement with the observation that the thermalizing population dominates the luminescence signal. In the  $x$ -direction, spatial coherence is lower than in the  $y$ -direction over the whole pump range. However, the condensate clearly exhibits high spatial coherence also in  $x$ -direction, in contrast to lasing, which shows separated emission stripes in the real space image (see Fig. 4d and Fig. S5). The spatial coherence measurements are in line with the observations from the 2D  $k$ -space images (Fig. 3), where 1) lasing exhibits confined luminescence along  $k_y$  (the direction of feedback) but spreads along  $k_x$ , 2) condensation shows 2D  $k$ -space confinement.

The lasing and condensation take place at energies 1.397 and 1.403 eV, respectively, lower than the band edge energy of the system without molecules, 1.423 eV. However the energies are blue-shifted from the lower polariton energy 1.373 eV (band edge in reflection) or 1.382 eV (fitted lower polariton branch; Fig. 1d), which are experimentally obtained by a reflection measurement and coupled modes model (35). Since the whole dispersion gradually blue shifts as a function of pump fluence, it may be associated to degradation of strong coupling instead of polariton-polariton interactions. Based on the band-edge locations (1.423 – 1.403) eV / (1.423 – 1.373) eV, the coupling in the condensation regime has decreased to  $\sim 40\%$  of the case without pumping. Note that the observed double-threshold behaviour is different from semiconductor microcavity polariton condensates where condensation has a lower threshold than photonic lasing associated with loss of strong coupling (16, 31).

## Stimulated nature of the thermalization

At the intermediate regime, we observed red shift of the luminescence as a function of distance in  $y$ -direction, Fig. 2e. The trails of the red shift begin from the emission maximum of the dye molecule ( $\sim 1.46$  eV), at a certain distance from the array edges, and reach the band edge energy ( $\sim 1.40$  eV) exactly at the center of the  $100 \times 100 \mu\text{m}^2$  array.

To understand the red shift, we have recorded real space images and spatially-resolved spectra for different lattice sizes at intermediate pump fluences sufficient to trigger the thermalization process, Fig. 5a-f. In a large array (Fig. 5-e-f), we observe the trails of the red shift toward the center of the array, similarly as in the  $100 \times 100 \mu\text{m}^2$  array (Fig. 2d-e), but the red-shifting populations do not merge at the center. In a small array (Fig. 5a-b), the situation looks different at first glance since the red shift seems to occur from the center of the array toward the edges. However, careful comparison of the distance between the array edge and the location where the red shift begins reveals that for all arrays, for the given pump fluence, the distance is the same ( $\sim 25 \mu\text{m}$ ; see Fig. 5a,c,e for definition of the distance).

We explain this distance by stimulated emission pulse build-up time: the time between the maxima of the population inversion and the output pulse as defined in the rate equation simulation in Fig. 5g (see Ref. (36) and Section S8 for description of the model). Pulse build-up is a well-known phenomenon in Q-switched lasers (37). In our system, the pump pulse excites the molecules, and the polaritons begin to propagate when the first spontaneous photons populate the modes. The modes then gather gain while propagating, and therefore the peak of the stimulated emission pulse appears after a certain distance travelled along the array. This distance is seen as the dark zones in real space measurements, and it corresponds to the pulse build-up time. Note that this pulse is different to a lasing or condensate pulse since the line width of the luminescence is large and spatial coherence is small. By summing up such spatial intensity profiles of the thermalizing pulses at every point along the lattice (Fig. 5h), we can reconstruct the real space intensity distributions (insets of Fig. 5a,c,e). The dark zones appear because the edges do not receive propagating excitations from outside the lattice; the dark zones at the edges have approximately half the intensity of the central part. In the small lattice, intensity at the edges is similar to that of the larger lattices but in the center it is only half

of that. Moreover the wavy interference patterns in the central part (Fig. 5c,e) indeed only appear for arrays larger than  $40 \times 40 \mu\text{m}^2$ , where there are counter-propagating pulses that can interfere.

We found that the width of the dark zones depends on pump fluence as predicted by the rate-equation simulation and the theory of Q-switched lasers, namely the build-up time is inversely proportional to the pump fluence. Fig. 5i shows that the dark-zone width follows the inverse of the pump fluence until it saturates at around  $3 \text{ mJ/cm}^2$  to a value below  $20 \mu\text{m}$  ( $\sim 100 \text{ fs}$ ). The inset in Fig. 5i shows the pulse build-up time extracted from our rate-equation simulation, and it displays a similar  $\sim 1/P$  dependence.

We attribute the red shift to a thermalization process. At the intermediate regime of pump fluences, however, a thermal distribution is not reached before the population decays. For higher fluences, a condensate peak and a tail with Maxwell-Boltzmann distributed population emerges. Emission-absorption cycles with dye molecules are known to provide thermalization of photons (19, 32, 38) and lattice plasmons (28), at the weak coupling regime, to the temperature of the vibrational degrees of freedom if several (39) (or at least one (20)) cycles take place within the cavity lifetime. In some studies of organic polariton condensates, condensation is attributed to loss of a vibrational quantum (14, 29, 40, 41). The SLR mode lifetimes are only about hundred femtoseconds, so it is unprecedented that we observe a prominent thermal distribution with dynamic range over one decade. We propose that this is possible because the thermalization is highly coherent due to the observed stimulated processes and due to strong light-matter coupling. For a single molecule with one vibrational state coupled to a few light modes, one can theoretically describe how a process that is coherent except for vibrational losses leads to rapid red shift of emission (Section S9). Describing quantum dynamics of molecules with thermal vibrational state populations, interacting strongly with multiple modes of light at the multi-photon regime, is beyond the current state-of-the-art theory (42–45). Such an advanced description will be needed to rigorously describe our observations.

## Effect of pulse duration

The spatial measurements have enabled an astounding, yet indirect, way to look into the dynamics of the system. To complement the spatial observations, we have probed the dynamics directly in the time domain by altering the excitation pulse duration. The pump fluences were kept constant so that the total amount of energy injected to the system per pulse is the same for different pulse durations. A 50 fs excitation pulse results in the double threshold behaviour with a distinct regime for lasing, an intermediate regime showing an incomplete stimulated thermalization process, and condensation, as explained above. Remarkably by using a longer pulse, we observe only the first (lasing) threshold, and the system does not undergo condensation even at higher pump fluences. The real space intensity distribution and spectrum remain almost unchanged from low to high pump fluence for a 500 fs pulse duration, Fig. 6. The intensity distributions and spectra resemble the lasing regime seen at low pump fluence with the 50 fs pulse (Fig. 2b-c), while the intermediate and condensation regimes are absent. Besides the luminescence intensity, the different threshold behaviour is clearly visible in the FWHM curves of the spectral maximum (Fig. S8). The FWHM is significantly decreased with both pulse durations at the first (lasing) threshold but only with the 50 fs pulse, the FWHM is decreased even further at the second (condensation) threshold. The  $k$ -space images and spectra for the 500 fs pulse (Fig. S9) reveal that the luminescence from low to high pump fluences is spread widely in the TM mode, hence there is no 2D confinement.

We have further studied the dependence on pulse duration by several intermediate measurements (Fig. S10) that show the critical pulse duration for condensation is around 100–250 fs. Interestingly this is similar to or smaller than the time ( $\sim 250$  fs) in which the polaritons propagate from the edges to the center in the  $100 \times 100 \mu\text{m}^2$  array. For a 250 fs pulse duration, some narrow peaks occur at the band edge but the thermalization in the time-integrated signal remains incomplete (too much population in the higher energy states), which can be because of molecules are brought to the excited state also during the thermalization process. With the longest excitation pulses ( $> 350$  fs), it seems the instantaneous population inversion does not reach a high enough value to even start the thermalization process as it competes from the same gain with the lasing, already triggered at the first threshold (see also Fig. 6). Sensitivity to the

excitation pulse duration highlights the ultrafast nature of plasmonic systems and endorses the sub-picosecond dynamics of the thermalization process. Besides the critical pulse duration, the condensation requires that the thermalization time matches the propagation time so that the polaritons have red shifted to the band edge energy while still having large population density, which can be achieved with an optimal balance between the dye concentration, lattice size, and periodicity.

## Conclusions

Fundamental questions on the dynamics of Bose-Einstein condensation in driven-dissipative systems are still largely open, despite years of research (*1, 2, 15, 16*). What is the nature of the energy relaxation and thermalization processes, how does the condensate form, and what are its quantum statistical and long-range coherence properties? These questions become challenging to answer for room temperature condensates as higher energy scales imply faster dynamics. Here we have shown that plasmonic lattices offer an impressive level of access and control to the sub-picosecond dynamics of condensate formation via propagation of excitations and the finite system size.

We experimentally demonstrated that a bosonic condensate with a clear-cut thermal excited state population can form in a timescale of a few hundreds of femtoseconds. We propose that this extraordinary speed of thermalization is possible because the process is partially coherent due to strong light-matter coupling and stimulated emission. Strong light-matter coupling at the weak excitation limit was indicated by our reflection measurements. By varying the lattice size, we revealed the stimulated nature of the thermalization process. While strong light-matter coupling at the multi-photon regime is described by the Dicke model (*46*), to explain both the red shift and the thermal distribution we observed, one would need to involve vibrational degrees of freedom that are (strongly) coupled to the electronic ones as well as to a thermal bath. Work toward surmounting such theoretical challenges has already begun since systems where light and molecular electronic and vibrational states are strongly coupled have promise for lasing and condensation, energy transfer, and even modification of chemical reactions (*47, 48*). We have shown here that plasmonic lattices offer a powerful platform for studies of such ultrafast

light-matter interaction phenomena. The shape, size, and material of the nanoparticles can be accurately tuned, as well as the lattice geometry, composition of the unit cell, and the lattice size. This provides a large, controlled parameter space vital for testing and (dis)qualifying theoretical predictions. In particular, the dynamics can be accessed in complementary ways: through conventional time-domain techniques as well as indirectly via the propagation of excitations in the lattice.

## Acknowledgments

We thank Janne Askola for his help in intensity calibration of the spectrometer. We thank Jonathan Keeling and Kristín Arnardóttir for useful discussions. **Funding:** This work was supported by the Academy of Finland under project numbers 303351, 307418, and 318987, and by the European Research Council (ERC-2013-AdG-340748-CODE). This article is based on work from COST Action MP1403 Nanoscale Quantum Optics, supported by COST (European Cooperation in Science and Technology). Part of the research was performed at the Micronova Nanofabrication Centre, supported by Aalto University. The Triton cluster at Aalto University (Science-IT) was used for computations. A.J.M acknowledges financial support by the Jenny and Antti Wihuri Foundation. K.S.D. acknowledges financial support by a Marie Skłodowska-Curie Action (H2020- MSCA-IF-2016, project id 745115). **Author contributions:** P.T. initiated and supervised the research. A.I.V. fabricated the samples. A.I.V., A.J.M., and K.S.D. conducted the experiments. A.J.M., A.I.V., P.T., and T.K.H. did the data analysis. A.I.V. performed the rate-equation, A.I.M. the quantum model, and M.N. the T-matrix calculations. A.I.V., A.J.M., and P.T. wrote the manuscript with all authors. **Competing interests:** The authors declare no competing financial interests. **Data and materials availability:** All data needed to evaluate the conclusions in the paper are present in the paper or the supplementary materials.

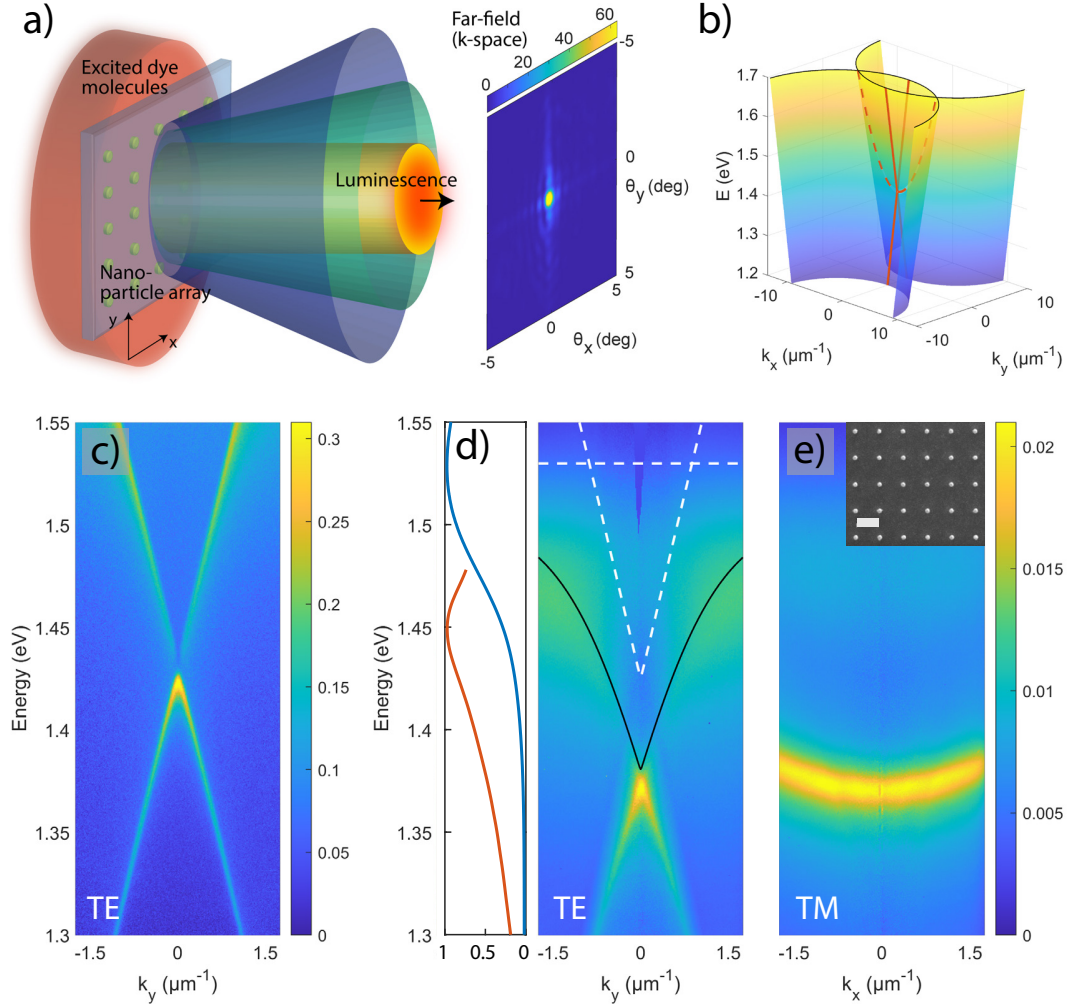


Figure 1: **Schematic of the system and dispersion of the modes.** (a) Artistic illustration of the experimental configuration. (b) Light cones for the diffracted orders (0,-1) and (0,+1) that arise for  $x$ -polarized nanoparticles. Crosscut along  $k_y$  ( $k_x = 0$ ) is called the TE mode (red solid lines) and along  $k_x$  ( $k_y = 0$ ) the TM mode (red dashed line). For the TE mode, the polarization is perpendicular to the propagation direction ( $\mathbf{e}_x, k_y$ ), and for the TM mode parallel ( $\mathbf{e}_x, k_x$ ). Crosscuts of the SLR dispersions are experimentally obtained by measuring the transmission (c) without the molecule or (d-e) reflection with 80 mM solution of IR-792. In (d), the SLR dispersion exhibits a red-shift and an avoided crossing with the absorption transition of the molecule. The absorption line and the uncoupled SLR mode are depicted with white dashed lines and the lower-polariton branch given by a coupled-modes-model fit is shown with a black line. Absorption and emission spectra of IR-792 are displayed in the left panel with blue and red lines, respectively. Scanning electron micrograph of the nanoparticle array is shown as an inset in (e), the scale bar is 500 nm.

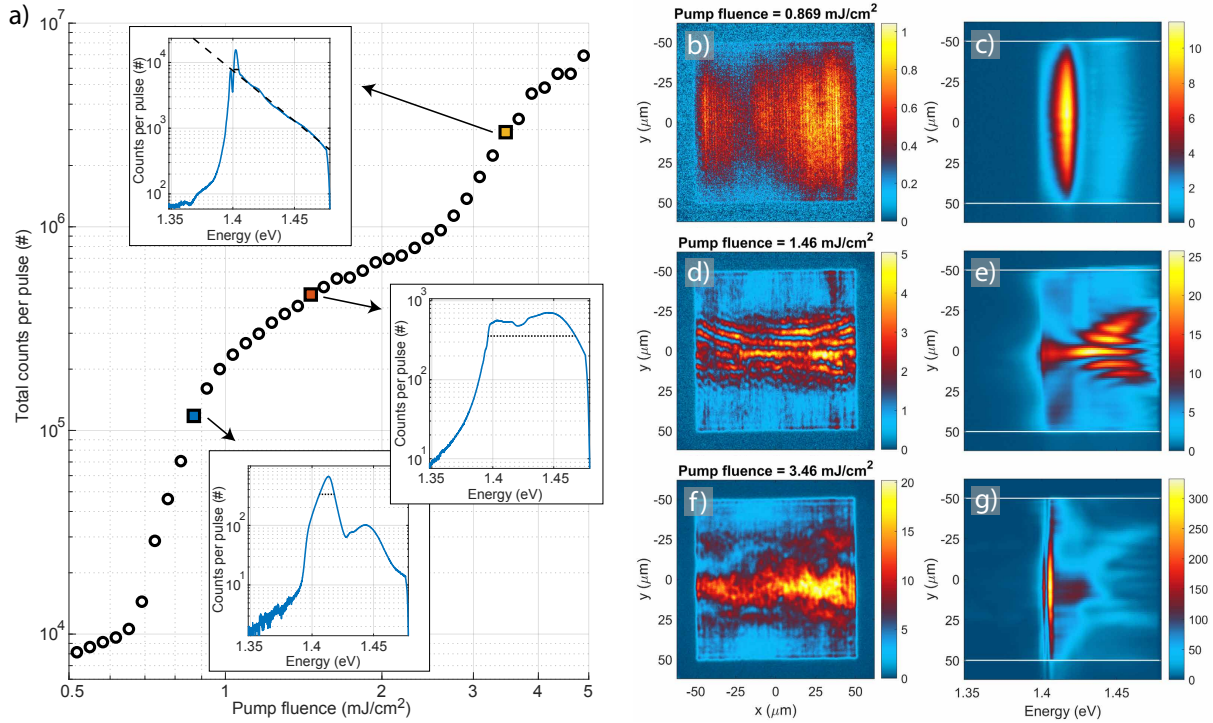


Figure 2: **Pump fluence dependence, real space images and spectra.** (a) Double-threshold curve of the pump fluence dependence of the total luminescence intensity. Inset: Line spectra obtained by integrating over the real space spectra in the  $y$ -direction (between the white lines). The FWHM of the spectral peaks is marked in the insets: 12 meV, 72 meV and 4.0 meV with increasing pump fluence. The dashed line in the top inset is a fit to the Maxwell–Boltzmann distribution which gives a temperature of  $333 \pm 12$  K (95% confidence bounds). (b-g) Left column: Real space images of the plasmonic lattice. Right column: Spectral information of the luminescence as a function of  $y$ -position. The pump fluence is: (b-c)  $0.87 \text{ mJ/cm}^2$ , (d-e)  $1.5 \text{ mJ/cm}^2$ , (f-g)  $3.5 \text{ mJ/cm}^2$ . The wave fronts in (d-e) arise from standing waves related to the momentum of the modes, for more information see Section S5. The real space images are recorded for single pump pulses but the corresponding spectra are integrated over 500 (c,e) and 70 pulses (g).

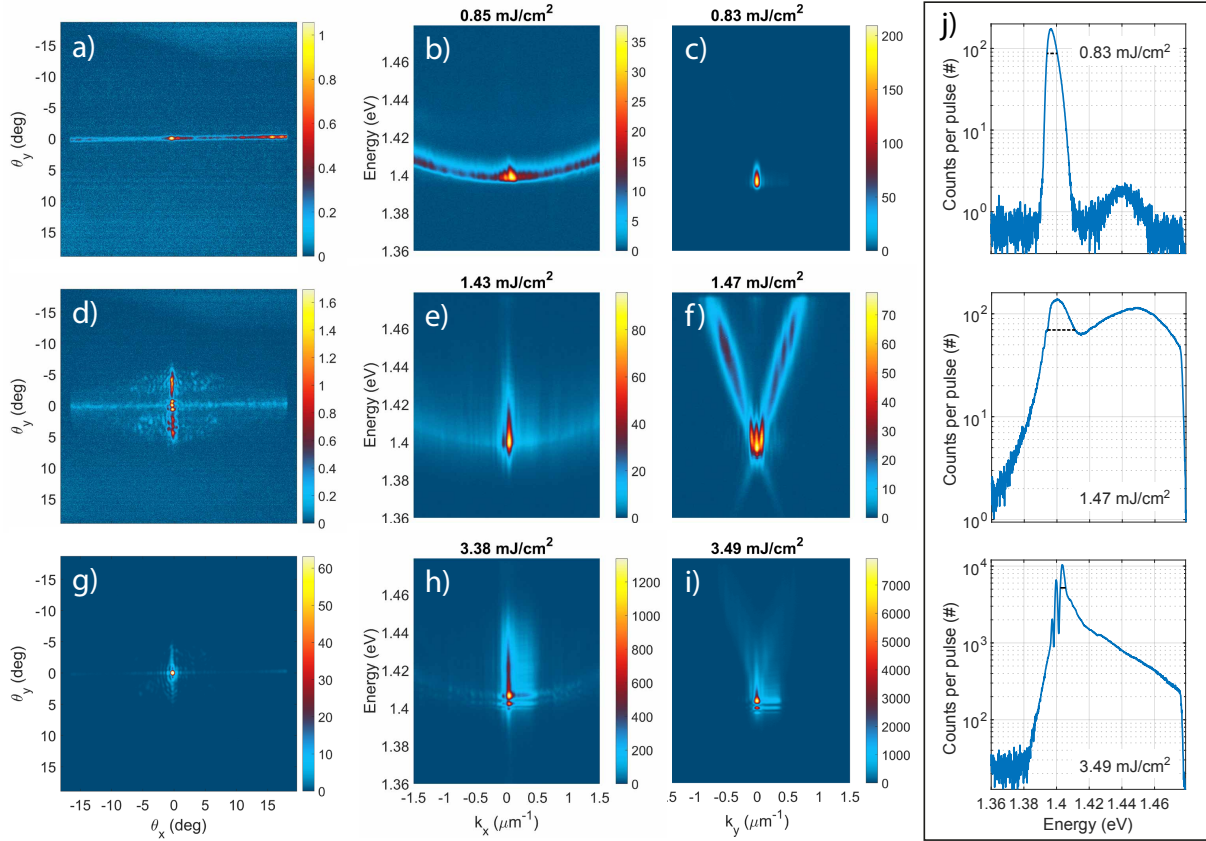
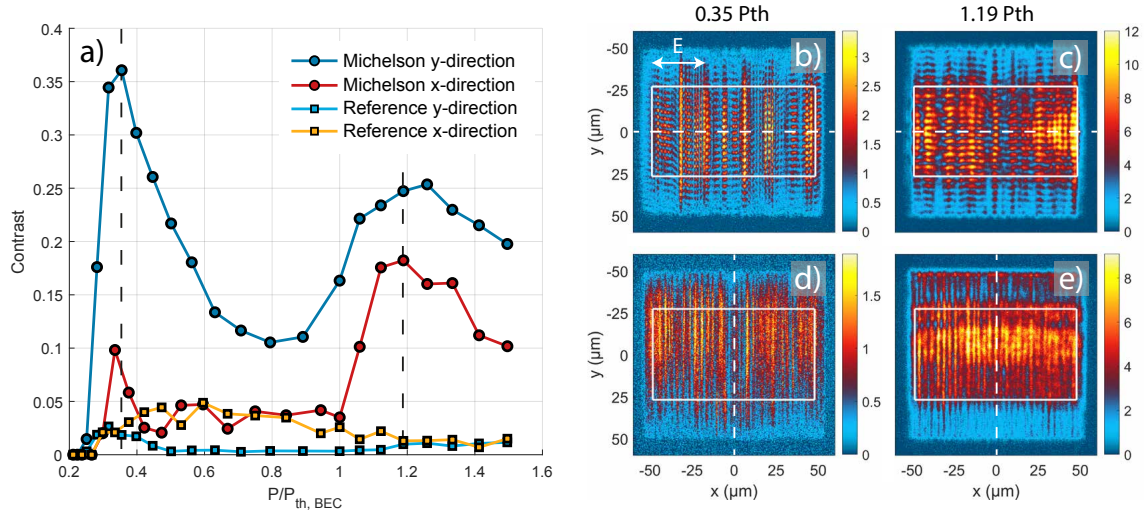
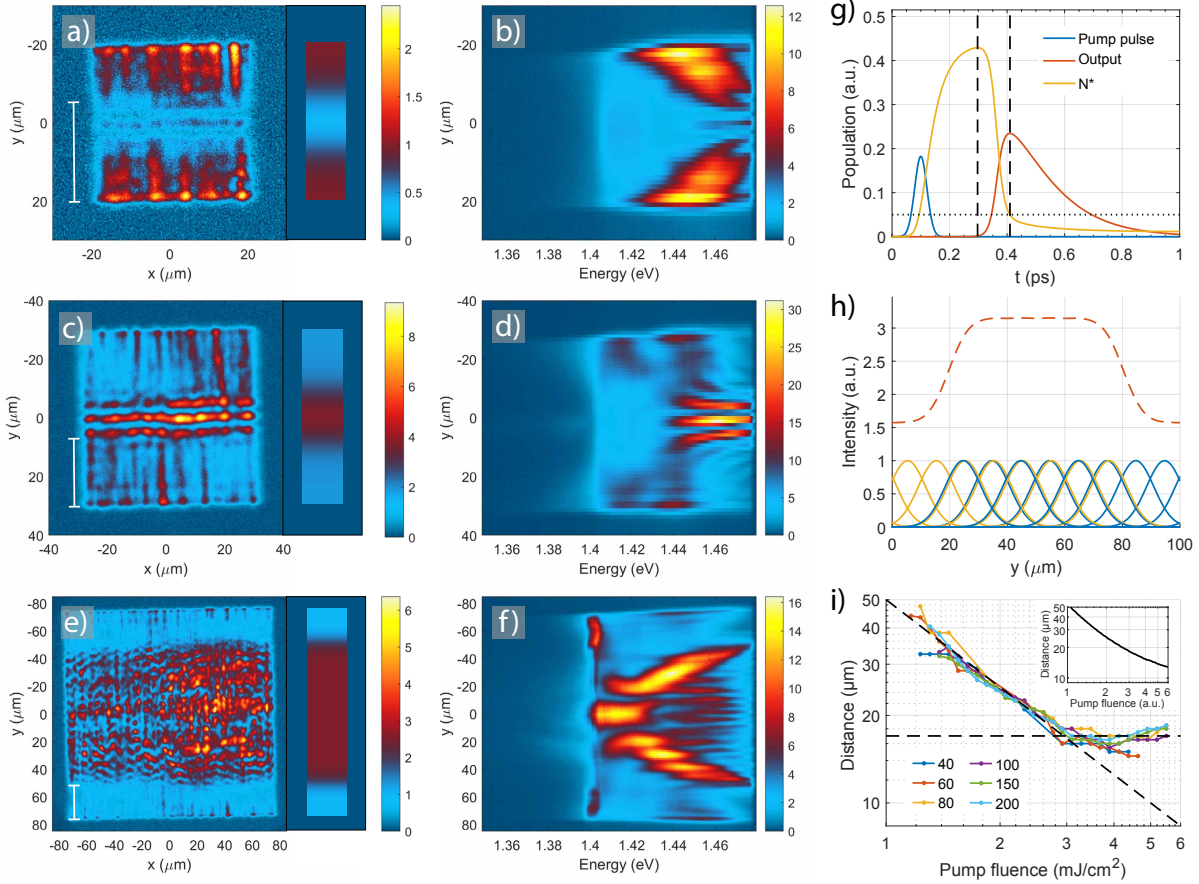


Figure 3: **Momentum space images and spectra.** First column: 2D momentum ( $k$ -)space images. Second and third column:  $k$ -space spectrum in the TM and TE mode directions, respectively. The spectra of the TM and TE modes correspond to horizontal and vertical slices of the 2D  $k$ -space spectrum, respectively. The pump fluence is: (a-c)  $0.85 \text{ mJ/cm}^2$ , (d-f)  $1.5 \text{ mJ/cm}^2$ , (g-i)  $3.5 \text{ mJ/cm}^2$ , as in Fig. 2. The horizontal stretching of the emission peaks in (h-i) are CCD blooming artifacts. (j) Population distribution in the TE mode integrated from (c,f,i) along  $k_y$ . FWHMs are indicated with dashed black lines:  $6.3 \text{ meV}$ ,  $17 \text{ meV}$  and  $3.3 \text{ meV}$  with increasing pump fluence.



**Figure 4: Spatial coherence measurement along  $y$  and  $x$ -axis of the plasmonic lattice.** (a) The fringe contrast over the region of interest (white boxes in (b-e)) as a function of pump fluence. For reference, the contrast is extracted also from non-interfered real space images, as light blue and yellow curves (details in Section S7). (b-e) Interfered real space images, where one of the images is inverted with respect to the white dashed line, to obtain the spatial coherence between  $-y$  and  $+y$  positions (b-c) or  $-x$  and  $+x$  positions (d-e). The interference patterns are shown for pump fluences corresponding to the lasing and condensation regimes (dashed lines in (a)). To obtain the spatial coherence between  $-x$  and  $+x$  positions, instead of rotating the detection optics, we rotate the sample (the lattice) and pump polarization by  $90^\circ$  (see Section S7). The real space images are recorded for single pump pulses.



**Figure 5: Observation of stimulated emission pulse build-up in finite size lattices.** a)-f) Real space images (left column) and spectra (middle column) at intermediate pump fluence ( $2.2 \text{ mJ/cm}^2$ ) for lattice sizes (a-b)  $40 \times 40 \text{ } \mu\text{m}^2$ , (c-d)  $60 \times 60 \text{ } \mu\text{m}^2$ , (e-f)  $150 \times 150 \text{ } \mu\text{m}^2$ . (g) Rate-equation simulation of stimulated emission. The pulse build-up time relevant for our system is marked by vertical dashed lines (the peaks of the population inversion  $N^*$  and of the output pulse). Horizontal dotted line indicates the value at which  $N^*$  overcomes the losses in the simulation. (h) Illustration of the sum (red dashed line) of spatial intensity profiles of the thermalizing pulses propagating to left (yellow) and right (blue) starting from everywhere along the  $y$ -axis of the array. The Gaussian shape approximates the increasing and decreasing intensity of the excitations as they gather gain and suffer losses under propagation. The results of such sum for different array sizes are shown as insets in (a,c,e) with the same false color as the real space images. (i) Measured distance from the array edge to the location where the red-shift begins (indicated by white lines in (a,c,e)) as a function of pump fluence for different lattice sizes. The legend indicates the square-array sizes in  $\mu\text{m}$ . The diagonal dashed line is the inverse of the pump fluence ( $50/P$ ), and the horizontal dashed line indicates the saturation value ( $\sim 18 \mu\text{m}$ ). The inset shows the pulse build-up time (converted to distance by multiplying with the group velocity of the SLR mode) obtained from the rate-equation simulation.

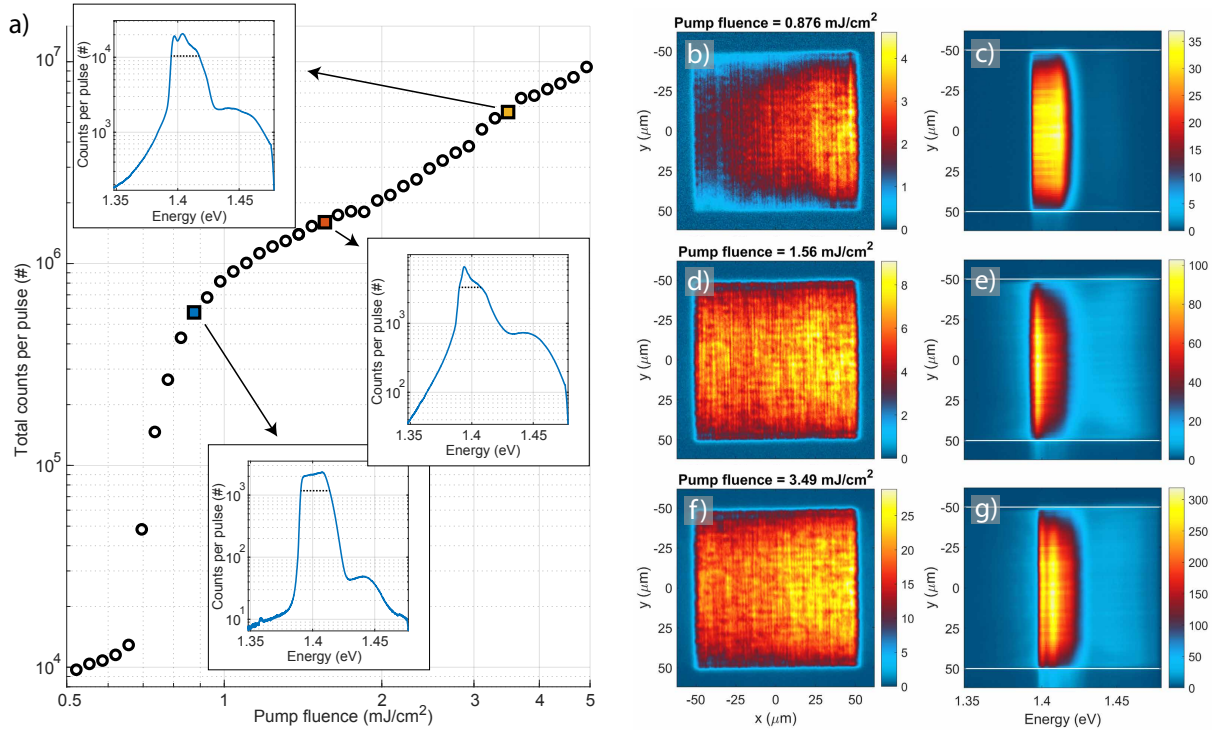


Figure 6: **Pump fluence dependence, real space images and spectra for 500 fs pump pulse duration.** (a) Pump fluence dependence of the total luminescence intensity. Insets: Line spectra obtained by integrating over the real space spectra in the  $y$ -direction (between the white lines). (b-g) Left column: Real space images of the plasmonic lattice. Right column: Spectral information of the luminescence as a function of position in the  $y$ -axis. The pump fluence is: (b-c) 0.88  $\text{mJ}/\text{cm}^2$ , (d-e) 1.6  $\text{mJ}/\text{cm}^2$ , (f-g) 3.5  $\text{mJ}/\text{cm}^2$ . FWHM of the spectral peaks is marked in the insets. With increasing pump fluence, we obtain a FWHM of 23 meV, 18 meV, and 23 meV.

## List of Supplementary materials

Section S1. Samples

Section S2. Transmission, reflection, and luminescence measurement setup

Section S3. Fits to the Maxwell–Boltzmann distribution

Section S4. Estimation of photon number in the condensate

Section S5. Band-edge energy

Section S6. T-matrix simulation

Section S7. Spatial coherence measurements

Section S8. Rate-equation simulation of a stimulated-emission pulse

Section S9. Description of the quantum model

Section S10. Different pump pulse durations

Fig. S1. Zoomed-in scanning electron microscope image of a nanoparticle array.

Fig. S2. Schematic of the experimental setup.

Fig. S3. Effect of the band-edge energy.

Fig. S4. Results of the T-matrix simulation for infinite arrays of nanoparticles.

Fig. S5. Spatial coherence measurement along  $y$  and  $x$  axis of the plasmonic lattice, with incoherently summed reference images.

Fig. S6. Fourier analysis method for extracting the fringe contrast in the Michelson interferometer images.

Fig. S7. Results of the quantum model.

Fig. S8. Pump fluence dependence and line spectra for 50 fs and 500 fs pulse durations.

Fig. S9. Real space and  $k$ -space measurement with pulse duration of 500 fs.

Fig. S10. Pump fluence dependence and line spectra for different pulse durations.

## Section S1. Samples

The gold nanoparticle arrays are fabricated with electron beam lithography on glass substrates where 1 nm of titanium is used as an adhesion layer (see SEM image in Fig. S1). The nominal dimensions of the plasmonic lattice, optimized for the condensation experiment, are the following: a nanoparticle diameter of 100 nm and height of 50 nm, the period in  $y$ - and  $x$ -direction of  $p_y = 570$  and  $p_x = 620$  nm, respectively, and a lattice size of  $100 \times 100 \mu\text{m}^2$ . In reference measurements, the period  $p_y$  is varied between 520 and 590 nm and the lattice size between  $40 \times 40$  and  $200 \times 200 \mu\text{m}^2$ .

Asymmetric periodicity separates the diffracted orders in the energy spectrum for the two orthogonal polarizations ( $e_x$  and  $e_y$ ), and the SLR dispersions are correspondingly separated, which simplifies the measured spectra. For  $x$ -polarized nanoparticles (as in our experiments), the TE and TM modes correspond to combinations of  $(e_x, k_y)$  and  $(e_x, k_x)$ , respectively. Under pumping, which SLR mode is mainly excited is determined by the pump polarization as the molecules are excited more efficiently via the single particle resonance at the plasmonic hot-spots of each nanoparticle (49). In the experiment with different periods,  $p_x$  was kept always 50 nm larger than  $p_y$ . In the experiment where lattice size was varied, however, the lattice period in  $x$  and  $y$  directions was the same ( $p_x = p_y = 570$  nm). We found that asymmetric periodicity does not play a crucial role in forming the condensate but just simplifies the data analysis of the experimental results.

The dye molecule solution is index-matched to the glass substrate ( $n = 1.52$ ), the solution being a mixture of 1:2 DMSO:Benzyol Alcohol. The solution is sealed inside a Press-to-Seal silicone isolator chamber (Sigma-Aldrich) between the glass substrate and superstrate. The dye solution has a thickness of  $\sim 1$  mm, which is very large compared to the extent of the SLR electric fields. Active region of the dye lies within a few hundred nanometers from the lattice plane, shown experimentally in (27, 36). Given by the excess of the dye molecules and the natural circulation of the fluid, there are always fresh dye molecules available for each excitation pulse, which makes the sample extremely robust and long-lasting. IR-792 perchlorate ( $C_{42}H_{49}ClN_2O_4S$ ) was chosen as the dye molecule because it dissolves to the used solvent in very high concentrations, in contrast to many other dye molecules, e.g., IR-140 that has also

been used by us (27, 36) and others (24, 26, 49) as a gain medium in plasmonic nanoparticle array lasers.

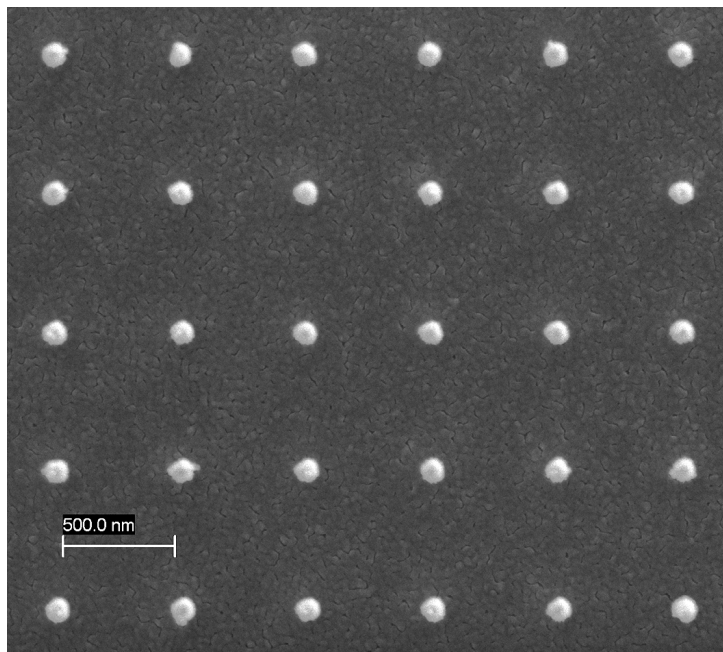


Figure S1: **Zoomed-in scanning electron microscope image of a nanoparticle array.** The same image is shown as an inset in manuscript Fig. 1.

## Section S2. Transmission, reflection, and luminescence measurement setup

A schematic of our experimental setup is depicted in Fig. S2. The same setup is used for transmission, reflection and luminescence measurements with minor modifications. The spectrometer resolves the wavelength spectrum of light that goes through the entrance slit, and each pixel column in the 2D CCD camera corresponds to a free space wavelength,  $\lambda_0$ , and each pixel row to a  $y$ -position at the slit. The  $y$ -position further corresponds to either an angle ( $k$ -space) or the  $y$ -position at the sample (real space). The photon energy is  $E = hc/\lambda_0$  and in the case of angle-resolved spectra (dispersions) the in-plane wave vector  $k_{x,y} = k_0 \sin(\theta_{x,y}) = 2\pi/\lambda_0 \sin(\theta_{x,y})$ , where  $h$  is the Planck constant and  $c$  the speed of light in free space. Next, the three different experiment types are explained, starting with the luminescence measurement where the sample is optically excited with an external pump laser.

The excitation pulse (or pump pulse) is generated by Coherent Astrella ultrafast Ti:Sapphire amplifier. The pulse has a central wavelength of 800 nm, and at the laser output, a duration of  $< 35$  fs with a bandwidth of 30 nm. The pump pulse is guided through a beam splitter and mirrors, and finally to the mirror  $M1$  (see Fig. S2), which directs the pump pulse to the excitation path of the setup. We have a band-pass filter in the excitation path that is used in combination with a long-pass filter in the detection path to filter out the pump pulse in the measured luminescence spectra. The pump pulse is linearly polarized, and to filter only the horizontal component we have placed a linear polarizer after the band-pass filter. The pump fluence is controlled with a metal-coated continuously variable neutral-density filter wheel (ND wheel). The pump pulse is spatially cropped with an adjustable iris and the iris is imaged onto the sample with a help of lens  $L1$  and the microscope objective. The inverted design enables exciting the sample at normal incidence, which is crucial for simultaneous excitation of the dye molecules over the sample. Excitation at normal incidence also prevents any asymmetry in the spatial excitation of the molecules around the nanoparticles with respect to lattice plane. The inverted pumping scheme and accurate optical alignment were essential for repeatable and precise condensate formation.

In the detection path, we have the long-pass filter and optionally a linear polarizer. An iris or pinhole acts as a spatial filter at the 1st image plane to restrict the imaged area at the sample. The 1st image plane is relayed onto the real-space camera (1st Cam.). In the  $k$ -space measurements, the back-focal plane of the objective (Fourier plane; containing the angular information of the collected light) is imaged to the 2nd Cam., that acts as a 2D  $k$ -space camera, and to the spectrometer slit, with the tube lens and a  $k$ -space lens. For the real space measurements, the beam-splitter before the  $k$ -space lens is replaced with an additional real-space lens to produce the 2nd image plane of the sample to 2nd Cam. and onto the spectrometer slit. The spectrometer slit selects a vertical slice either of the 2D  $k$ -space image or the real space image. In the luminescence measurements, we use a slit width of  $500 \mu\text{m}$ . In the  $k$ -space, it corresponds to  $\pm 1.3^\circ$  around  $\theta_x = 0$ , or to  $\pm 0.16 \mu\text{m}^{-1}$  around  $k_x = 0$  at  $E = 1.4$  eV. Respectively in the real space, the slit opening of  $500 \mu\text{m}$  corresponds to  $27 \mu\text{m}$  slice at the sample.

The dispersion of optical modes in the bare plasmonic lattice can be measured in transmission mode of the setup, where the sample is illuminated with a focused and diffused white light

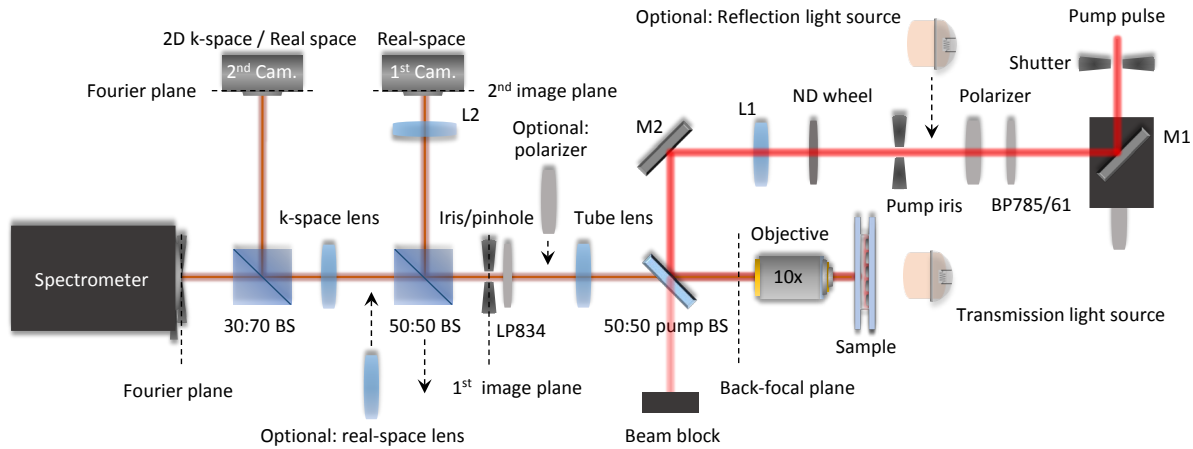


Figure S2: **Schematic of the experimental setup.** The setup allows acquiring the real space,  $k$ -space, and spectral information simultaneously, and it is modular to measuring transmission, reflection, and the luminescence properties of the sample. Here, BP 785/61 refers to a band-pass filter with a bandwidth of 61 nm centered at 785 nm, LP 834 refers to a long-pass filter with a cutoff at 834 nm, M stands for mirror, L for lens, ND for neutral density, and BS stands for a beam splitter with a marked fraction of (R:T).

from a halogen lamp. The lattice modes are visible as transmission minima (extinction maxima) in the angle-resolved spectrum. When a thick layer of high-concentration dye molecule solution is added in the chamber on top of the nanoparticle array, the transmission measurement is not applicable due to a complete absorption by the molecules. To access the dispersion of the lattice modes in this case, we use the setup in reflection mode by utilizing the same inverted design as in the luminescence measurement. The halogen lamp is inserted before the iris in the excitation path, that is imaged onto the sample, and the dispersion of the lattice modes is revealed by reflection (scattering) maxima in the collected angle-resolved spectrum.

The luminescence measurement as a function of pump fluence is automated with LabView. Predefined fluence steps are measured such that for each step: 1) the calibrated ND filter wheel is set to a correct position, 2) the shutter is opened, 3) the image is acquired with spectrometer and optionally with 1st and 2nd Cam., and 4) the shutter is closed. Integration time of the spectrometer is automatically adjusted during the measurement to avoid saturation at highly non-linear threshold regimes. The pump pulse duration is measured with a commercial autocor-

relator (APE pulseCheck 50). In the pulse duration measurement, the pump pulse goes through the same optics as in the actual experiments. The pulse duration is changed by adjusting the stretcher-compressor of the external pump laser.

### Section S3. Fits to the Maxwell–Boltzmann distribution

We fit the thermalized tail in the measured population distributions to Maxwell–Boltzmann distribution (manuscript Fig. 2 and Fig. S8). The fit function is given by

$$f_{\text{MB}}(E) = \frac{d(E)}{e^{(E-\mu)/(k_{\text{B}}T)}}, \quad (1)$$

where  $d(E)$  is the degeneracy of the modes as a function of energy  $E$ ,  $\mu$  is the chemical potential,  $k_{\text{B}}$  is the Boltzmann constant, and  $T$  is temperature. The fit was done for the linear part of the distribution in logarithmic scale, at pump fluence above the threshold. Fitting was performed with a non-linear least squares method. The degeneracy  $d(E)$  was approximated by the density of states for a plane wave travelling in a 2D plane, which is linearly increasing but nearly constant ( $d(E) = 1 \dots 1.05$ ) for the fitted energy range of  $\sim 60$  meV.

The fit gives a temperature of  $333 \pm 12$  K for a chosen pump fluence of  $P = 3.5$  mJ/cm<sup>2</sup>, error limits representing the 95% confidence bounds for the fit. This fit is presented in manuscript Fig. 2a (top inset) and Fig. S8a. The fitted pump fluence is chosen such that the fluence is the lowest showing a linear slope in the time-integrated population distribution (in logarithmic scale). The chosen fluence also corresponds to the narrowest FWHM of the highest condensate peak (see Fig. S8c). The high-energy tail remains linear over pump fluences between  $\sim 3.5 \dots 4$  mJ/cm<sup>2</sup>, with a slightly changing slope. For two higher pump fluences of 3.7 and 3.9 mJ/cm<sup>2</sup>, the fits to the Maxwell–Boltzmann distribution give temperatures of  $291 \pm 7$  K and  $262 \pm 9$  K, respectively. For pump fluences above  $\sim 4$  mJ/cm<sup>2</sup>, the linear slope is distorted and the condensate degrades. This is evident also as a decrease of the spatial coherence (manuscript Fig. 4a) and an increase of the FWHM of the spectral maximum (Fig. S8c).

## Section S4. Estimation of photon number in the condensate

The photon number in the condensate is estimated from the measured luminescence intensity. A strongly attenuated beam from the external pump laser (800 nm, 1 kHz) is directed to the spectrometer slit, and the total counts given by the spectrometer CCD camera (Princeton Instruments PIXIS 400F) is compared to the average power measured with a power meter (Ophir Vega). The measured average power of 167 nW corresponds to  $6.7 \cdot 10^8$  photons/pulse whereas the total counts in the CDD camera are  $8.4 \cdot 10^6$ , leading to a conversion factor of  $\sim 80$  photons/count. In the condensation regime, the total counts per pulse is about  $3 \cdot 10^6$  (manuscript Fig. 2a). The collection optics including the beam splitters reduce the signal roughly by a factor of 2.5, and as the slit width of 500  $\mu\text{m}$  corresponds to 27  $\mu\text{m}$  at the sample, we collect luminescence from an area that is about 1/4 of the 100  $\mu\text{m}$  wide nanoparticle array. Finally, the sample is assumed to radiate equally to both sides, so the actual photon number per emitted condensate pulse becomes:  $n_{ph} \approx 2.5 \times 4 \times 2 \times 80 \times 3 \cdot 10^6 = 4.8 \cdot 10^9$ .

## Section S5. Band-edge energy

We demonstrate the effect of the band edge location in Fig. S3 with two examples where the band edge is tuned either below or above the optimal energy of 1.40 eV. When the periodicity is set small so that the band edge of the  $x$ -polarized TE mode is at high energy (Fig. S3a-c), the propagation and red shift occurs along the lower dispersion branch of the TE mode, i.e., the red shift is not halted at the band edge. In contrast, when periodicity is set large so that the band edge resides at low energy (Fig. S3d-f), we observe the red shift of polaritons propagating along the upper dispersion branch of the TE mode but no condensation. The red-shifting population simply does not reach the band edge, which is at too low energy. The stripes in the real space spectra, Fig. S3b,e (also visible in manuscript Fig 2d,e and Fig. 4c-f), arise from standing waves caused by counter-propagating modes. We found that the wavelength of the intensity oscillations is  $\lambda_{RS}(E) = \pi/k(E)$ . Comparing the  $k$ -space and real space spectra shows in Fig. S3a-b that the oscillations are denser at lower energies because the lower energy corresponds to larger  $k$ . In contrast in Fig. S3d-e, the oscillations are sparser at lower energies because the lower energy corresponds to smaller  $k$ .

Interestingly while in previous studies using a dye molecule bath for photons (19, 32) or lattice plasmons (28) condensation required matching the lowest state energy with the energy where the molecule absorption vanishes, here that condition is not needed but the condensate formation is controlled by the interplay of the lattice size, periodicity and thermalization speed.

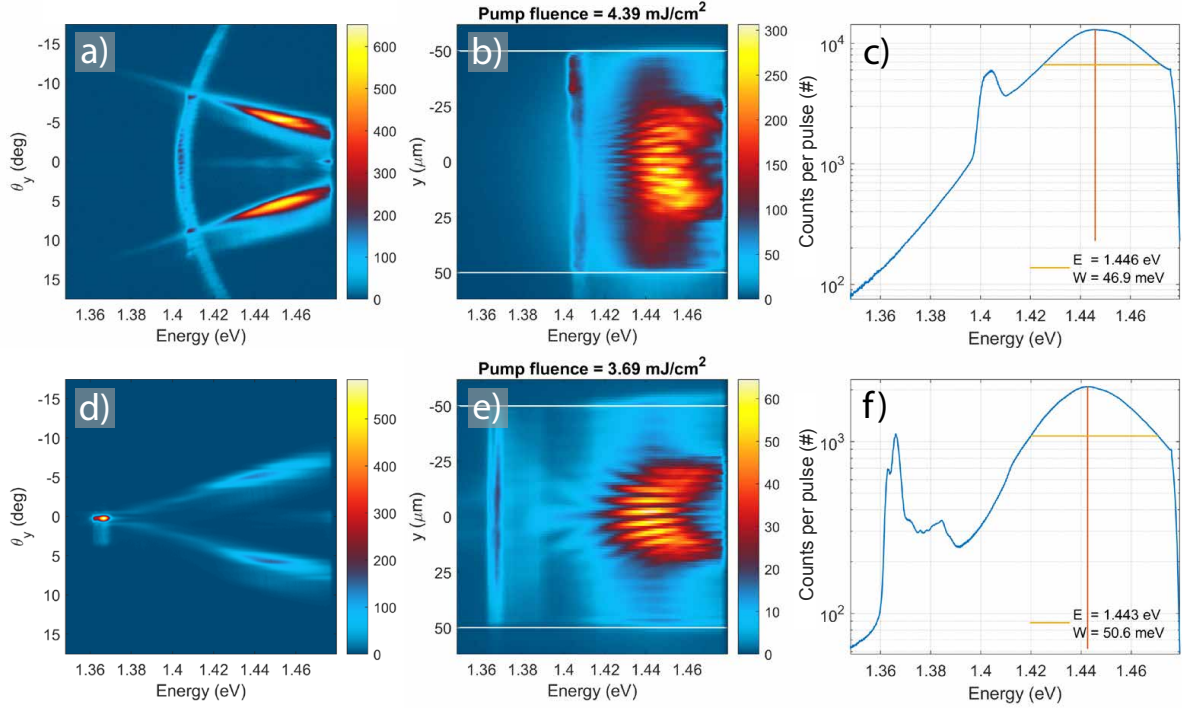


Figure S3: **Effect of the band-edge energy.** Left column:  $k$ -space spectra in the TE mode direction. Middle column: Real space spectra. Right column: Line spectra obtained by integrating over the real space spectra in  $y$ -direction (between white lines). Results are shown for two lattice periods: (a-c)  $p_y = 520$  nm and (d-f)  $p_y = 590$  nm. Note that in (a) the curved band visible at 1.40...1.42 eV is the TM mode of the  $y$ -polarized nanoparticles ( $p_x = 570$  nm).

## Section S6. $T$ -matrix simulation

To unveil the origin of the multiple modes, we have performed multiple-scattering  $T$ -matrix simulations of an infinite array of spherical nanoparticles, with the periods in  $x$  and  $y$  directions corresponding to our system.

In the  $T$ -matrix approach, the scattering properties of a single nanoparticle are first described

in terms of vector spherical wave functions (VSWFs), giving the  $T$ -matrix of the particle at a given frequency. For a spherical particle, the nontrivial elements of the  $T$ -matrix are given by the well-known Lorentz-Mie solution (50). Next, the interactions between nanoparticles at different positions are expressed in terms of translation operators between the VSWFs with different origins (51). Applying the Bloch boundary conditions, the electromagnetic response of a periodic nanoparticle array can be described with a matrix equation of the form

$$(I - TW)a = Tp_{\text{ext}} \quad (2)$$

where  $T = T(\omega)$  is the single particle  $T$ -matrix,  $W(\omega, \mathbf{k})$  is a lattice sum of the VSWF translation operators,  $a$  is a vector containing the coefficients of VSWFs scattered from a nanoparticle, and  $p_{\text{ext}}$  is a vector of incoming VSWF coefficients, describing the external fields driving the array. Lattice modes are defined as the solutions of Eq. (2) with the right hand side set to zero (physically this means the waves propagate without the need of external driving) and exist only for such  $(\omega, \mathbf{k})$  pairs for which the matrix  $(I - TW)$  is singular (giving the dispersion relation of the array), which is equivalent to some singular value of the matrix being equal to zero. In practice, the particles are lossy, hence the frequency  $\omega$  needs to be complex if the wave vector  $\mathbf{k}$  is real. We also exploit the symmetries of the system and evaluate the equation (2) separately for each irreducible representation of the little group corresponding to a given  $\mathbf{k}$  vector. This gives us additional a priori information about the multipole polarizations of the particles in different modes. For a more detailed description of the method, see the Supporting Information of Ref. (52).

Fig. S4 shows the singular values of  $(I - TW)$  for spherical nanoparticles of three different radii. For the smallest nanoparticle, the singular value minima (which correspond to the lattice modes) of all irreducible representations are concentrated at one energy. As the particle size is increased, some of the minima (hence also the modes) start to separate from each other in energy. The results show that multiple degenerate modes exist at  $k = 0$  for small particles, but larger particle size lifts this degeneracy producing closely spaced modes with non-uniform spacing, see Fig. S4. We conclude that the multi-peak structure of the condensate can thus originate from the complexity of finite-sized nanoparticles.

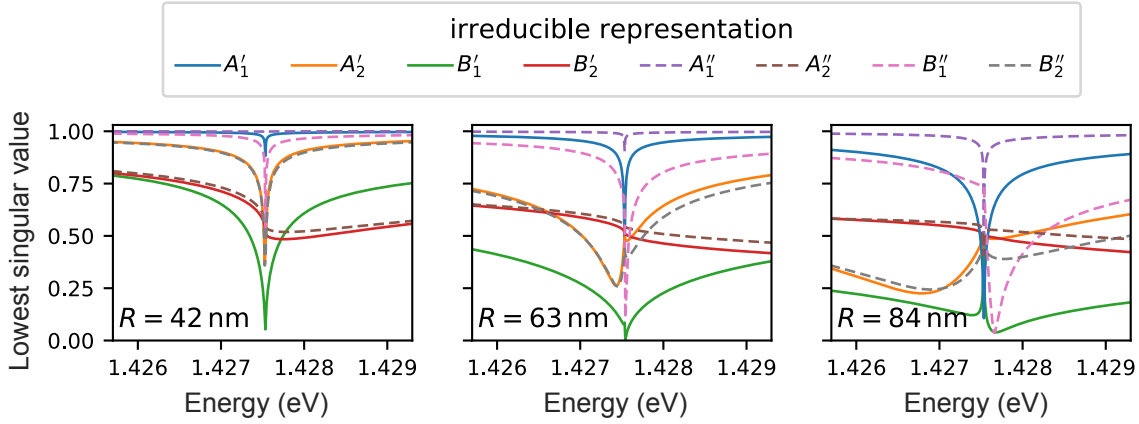


Figure S4: **Results of the T-matrix simulation for infinite arrays of nanoparticles.** Modes at  $k = 0$  of infinite rectangular arrays of spherical nanoparticles with periods  $p_x = 621$  nm,  $p_y = 571$  nm, and varying radii  $R$ , obtained by the multiple-scattering  $T$ -matrix method up to the octupole degree. Each line represents the lowest singular value of the left hand side of Eq. (2) projected onto an irreducible representation of the little group  $G_\Gamma \simeq D_{2h}$  of the lattice at the  $\Gamma$  point. A zero singular value represents a lattice mode. Note that the plots here are for real energies only, while the lattice mode energies are in fact complex due to ohmic losses, therefore the plots only approach zero without actually touching it.

## Section S7. Spatial coherence measurements

Spatial coherence of the sample luminescence is measured with a Michelson interferometer. The real space image is split into two arms and the image in one of the arms is inverted in vertical direction with a hollow roof retro-reflector. Then the two images are combined again with a beam splitter and overlapped at the camera pixel array, simultaneously. With this design the spatial coherence (first-order correlation  $g^{(1)}$ ) can be measured separately along both  $x$ - and  $y$ -axis of the plasmonic lattice. The retro-reflector always inverts the image vertically, with respect to  $y = 0$  in laboratory reference frame, but the sample and the pump polarization can be rotated  $90^\circ$  to measure  $g^{(1)}(-x, x)$  instead of  $g^{(1)}(-y, y)$  in the lattice coordinates. The first-order correlation function describing the degree of spatial coherence is given by

$$g^{(1)}(-\mathbf{y}, \mathbf{y}) = \frac{\langle E^*(-\mathbf{y})E(\mathbf{y}) \rangle}{\sqrt{\langle E(-\mathbf{y})^2 \rangle \langle E(\mathbf{y})^2 \rangle}}, \quad (3)$$

where  $E(\mathbf{y})$  is the electric field at point  $\mathbf{y}$ . The first-order correlation function relates to the interference fringe contrast  $C$  as follows:

$$C(\mathbf{y}, -\mathbf{y}) = \frac{2\sqrt{I(\mathbf{y})I(-\mathbf{y})}}{I(\mathbf{y}) + I(-\mathbf{y})}g^{(1)}(\mathbf{y}, -\mathbf{y}), \quad (4)$$

where  $I(\mathbf{y})$  is the luminescence intensity at point  $\mathbf{y}$  of the lattice. The fringe contrast in the interfered images is extracted with a Fourier analysis as explained below.

First we need to determine the period of the interference fringes arising due to coherence of  $E(\mathbf{y})$  and  $E(-\mathbf{y})$ , and set a Fourier filter for spatial frequencies accordingly. After that, the image data is gone through column by column, inside the region of interest, and a Matlab inbuilt Fast-Fourier Transform algorithm is performed to each pixel column at a time. In the spatial frequency spectrum, we find the peak value inside a predefined frequency bandwidth and compare that to the noise floor. The peak value needs to be above a chosen threshold value. If the peak is above the threshold, the rms-sum of the frequency components within the predefined bandwidth is compared to the background level (DC value of the frequency spectrum). Finally the contrast at certain pump fluence is taken as the mean value of the contrast along the columns inside the region of interest. The threshold value for a peak-acceptance level is adjusted so that the mean contrast value found in the reference cases (incoherently summed real space image) stays below 5%. Fig. S6 shows an explanatory example when the method is not applied for each pixel column separately but the intensity along  $y$ -axis averaged over  $x$  (from Fig. S5b), and the intensity along  $x$ -axis averaged over  $y$  (from Fig. S5d).

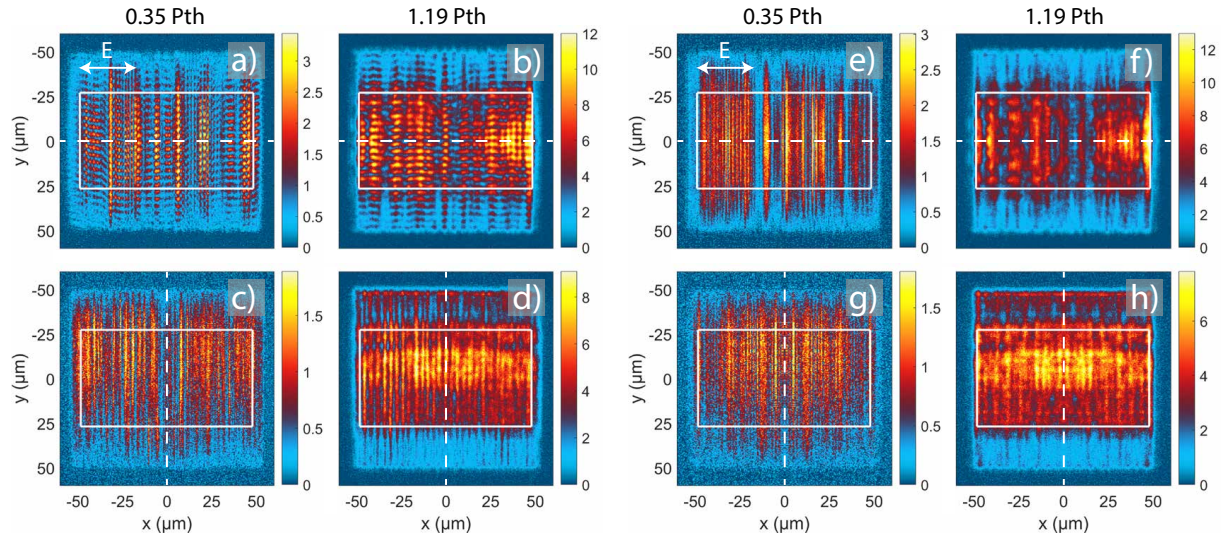
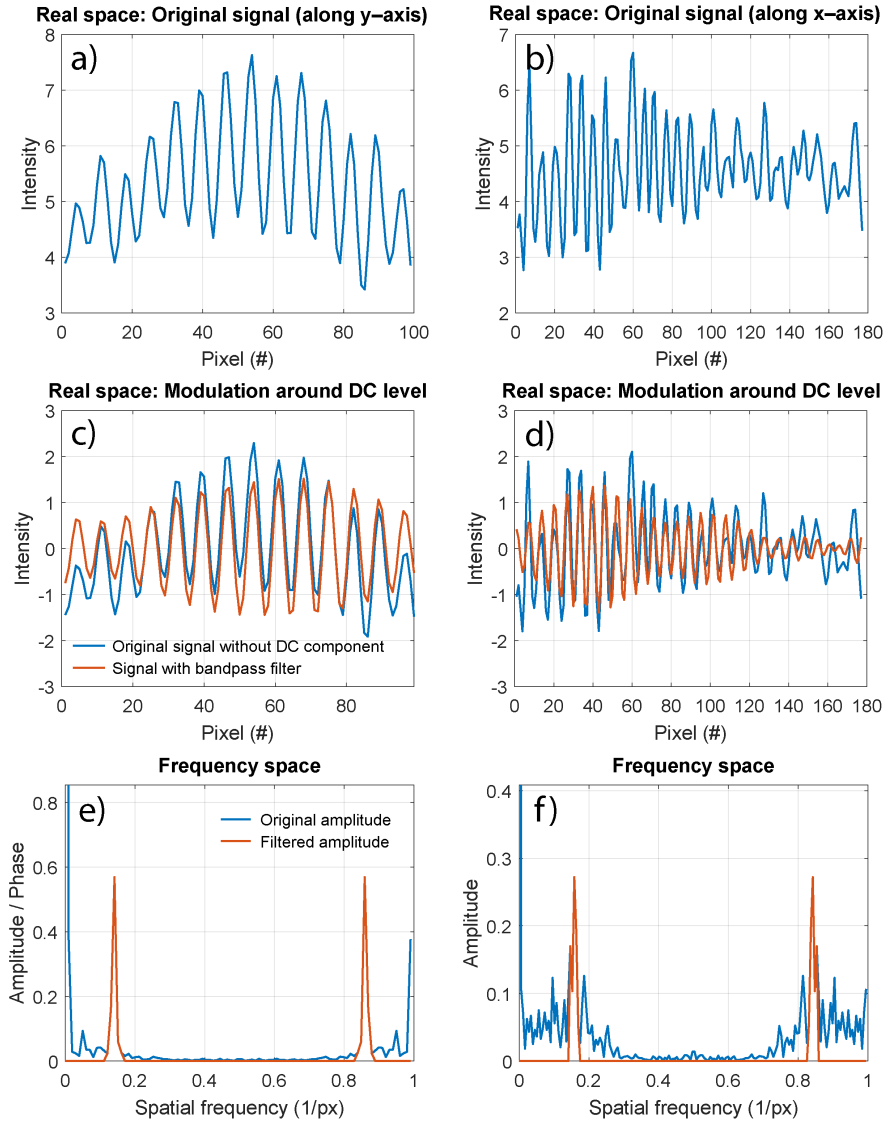


Figure S5: **Spatial coherence measurement along  $y$  and  $x$  axis of the plasmonic lattice, with incoherently summed reference images.** (a-d) show the same images as the manuscript Fig. 4, (e-h) show reference images for the same pump fluences. The reference images are obtained by inverting a real space image from one of the Michelson arms in the post processing, and summing it with the original non-inverted image. This is an incoherent equivalent of the coherently summed images in the Michelson interferometer. There is a clear difference between the interfered and non-interfered images in the  $y$ -direction coherence measurement (a,b,e,f) but not so clear in the  $x$ -direction measurement (c,d,g,h). For that, Fourier analysis of spatial frequencies is necessary to extracting the fringe contrast caused by spatial coherence. Here  $P_{th}$  means the threshold pump fluence for condensation and  $\mathbf{E}$  refers to the pump polarization. The real space images are recorded for single pump pulses.



**Figure S6: Fourier analysis method for extracting the fringe contrast in the Michelson interferometer images.** The left panel (a,c,e) shows the intensity along  $y$ -axis of the lattice, averaged over  $x$  (see white box in Fig. S5b), and the right panel (b,d,f) shows the intensity along  $x$ -axis of the lattice, averaged over  $y$  (Fig. S5d). In (c-f), the blue curves show the original signal and the red curves the filtered signal.

## Section S8. Rate-equation simulation of a stimulated-emission pulse

We use a standard four-level model for the gain medium to simulate the stimulated emission pulse when the four-level system is originally in its ground state, and excited with a 50 fs pump pulse. The levels are labeled as follows: the pump excites the system from the level 0 to 3, there is a non-radiative decay from 3 to 2, and emission to the cavity mode is from 2 to 1. The model shows the same temporal evolution after the pump pulse as a gain-switched laser, or a  $Q$ -switched laser after the  $Q$ -switch is opened (37). The transition lifetimes used for the four-level gain medium are:  $\tau_{32} = \tau_{10} = 50$  fs and  $\tau_{21} = \tau_{20} = 500$  ps, which are similar to those used in the literature for organic dye molecules (24, 27, 36). The spontaneous emission coupling factor ( $\beta$ -factor) is set to  $\beta = 0.001$  and the cavity lifetime to  $\tau_{cav} = 100$  fs (corresponding to a typical lifetime of an SLR mode). The model is defined with the following coupled rate-equations, as in Ref. (36):

$$\frac{dn_{ph}}{dt} = \beta n_{ph} \frac{(N_2 - N_1)}{\tau_{21}} + \beta \frac{N_2}{\tau_{21}} - \frac{n_{ph}}{\tau_{cav}} \quad (5)$$

$$\frac{dN_0}{dt} = -rN_0 + \frac{N_2}{\tau_{20}} + \frac{N_1}{\tau_{10}} \quad (6)$$

$$\frac{dN_3}{dt} = rN_0 - \frac{N_3}{\tau_{32}} \quad (7)$$

$$\frac{dN_2}{dt} = -\beta n_{ph} \frac{(N_2 - N_1)}{\tau_{21}} - \frac{N_2}{\tau_{21}} - \frac{N_2}{\tau_{20}} + \frac{N_3}{\tau_{32}} \quad (8)$$

$$\frac{dN_1}{dt} = \beta n_{ph} \frac{(N_2 - N_1)}{\tau_{21}} + \frac{N_2}{\tau_{21}} - \frac{N_1}{\tau_{10}}, \quad (9)$$

where the populations of each level are denoted with  $N_i$  and the transition lifetimes with  $\tau_i$ . Here,  $n_{ph}$  is the photon number in the mode (in our case the number of polaritons). Parameter  $r$  is the pump rate proportional to the pump intensity that has a Gaussian temporal shape.

In the model, the threshold value for population inversion is defined by comparing the gain and loss terms for the photon number in Eq. (5). The optical gain must overcome the loss, and at the threshold they are equal

$$\beta n_{ph} \frac{(N_2 - N_1)}{\tau_{21}} = \frac{n_{ph}}{\tau_{cav}}. \quad (10)$$

With a definition of  $N^* = N_2 - N_1$ , the threshold value becomes

$$N_{th}^* = \frac{\tau_{21}}{\beta\tau_{cav}}. \quad (11)$$

## Section S9. Description of the quantum model

We have studied the thermalization mechanism qualitatively with a microscopic quantum model including multiple cavity modes coupled to a single two-level system that is coupled to a shifted harmonic oscillator that describes the rotational-vibrational degrees of freedom within a molecule. The results of the model are presented in Fig. S7.

The system is described by the Holstein-Tavis-Cummings model (43,53–56) with the Hamiltonian ( $\hbar = 1$ )

$$H = \sum_i \omega_i a_i^\dagger a_i + \frac{\omega_m}{2} \sigma^z + \sum_i \left( g a_i \sigma^+ + g^* a_i^\dagger \sigma^- \right) + \omega_v b^\dagger b + \omega_v \sqrt{S} (b^\dagger + b) \sigma^z. \quad (12)$$

Here  $a_i^\dagger$  is the bosonic creation operator of the cavity mode of index  $i$ ,  $\sigma^z$  and  $\sigma^\pm$  are the Pauli operators describing the two-level structure of the molecule and  $b^\dagger$  is the bosonic creation operator corresponding to the vibrational mode of the molecule. Furthermore,  $\omega_k$  is the energy of the cavity mode of index  $i$ ,  $\omega_v$  is the energy of the vibrational mode,  $\omega_m$  is the energy of the two-level system,  $g$  is the coupling between cavity modes and the molecule, and  $S$  is the Huang-Rhys parameter. Rotating wave approximation has been used in the simulation, assuming that the coupling  $|g|$  is significantly smaller than the molecule and cavity mode frequencies. This is true with the parameters used in the simulation:  $\omega_i = 1.40, 1.41, 1.42, 1.43, 1.44, 1.45$ ,  $\omega_m = 1.45$ , and  $g = 0.0075$  (in eV). Other parameters in the Hamiltonian used in the simulation are:  $\omega_v = 0.03$  eV and  $S = 0.1$ .

Dissipations of an open quantum system are taken into account in the Lindblad formalism, which yields the master equation (57):

$$\begin{aligned} \frac{\delta\rho(t)}{\delta t} = & \frac{i}{\hbar} [\rho(t), H] + \sum_i \kappa_i \mathcal{L}[a_i] + \gamma_m \mathcal{L}[\sigma^-] + \gamma_z \mathcal{L}[\sigma^z] \\ & + \gamma_{v,+} \mathcal{L}[b^\dagger - \sqrt{S}\sigma^z] + \gamma_{v,-} \mathcal{L}[b - \sqrt{S}\sigma^z], \end{aligned} \quad (13)$$

where  $\mathcal{L}[O] = O\rho O^\dagger - \frac{1}{2}O^\dagger O\rho - \frac{1}{2}\rho O^\dagger O$  is the Lindblad superoperator,  $\kappa$  is the cavity dissipation rate,  $\gamma_m$  and  $\gamma_z$  are the radiative dissipation and dephasing rates of the molecule, and  $\gamma_{v,\pm}$

are the rates that describe thermal excitation (+) and dissipation (−) of the vibrational mode. These rates are  $\gamma_{v,+} = \gamma_v n_B$  and  $\gamma_{v,-} = \gamma_v (n_B + 1)$ , where  $n_B = 1/[\exp(\omega_v/k_B T_{\text{mol}}) - 1]$  is the occupation probability of the vibrational mode of energy  $\omega_v$  at thermal equilibrium. Solving Eq. (13) for  $\langle a_i^\dagger a_i \rangle$ ,  $\langle \sigma^z \rangle$ , and  $\langle b^\dagger b \rangle$  gives the time evolution of occupation of the cavity modes and the molecule as well as excitation of the vibrational mode. Parameters used in the simulation for Fig. S7 are  $\gamma_v = 4 \times 10^{-3}$ ,  $\gamma_m = 1 \times 10^{-6}$ ,  $\gamma_z = 1 \times 10^{-3}$ ,  $\kappa = 6 \times 10^{-3}$ , and  $T_{\text{mol}} = 25 \times 10^{-3}$  (in eV). The simulation was performed using Python 3 with QuTiP toolbox (58).

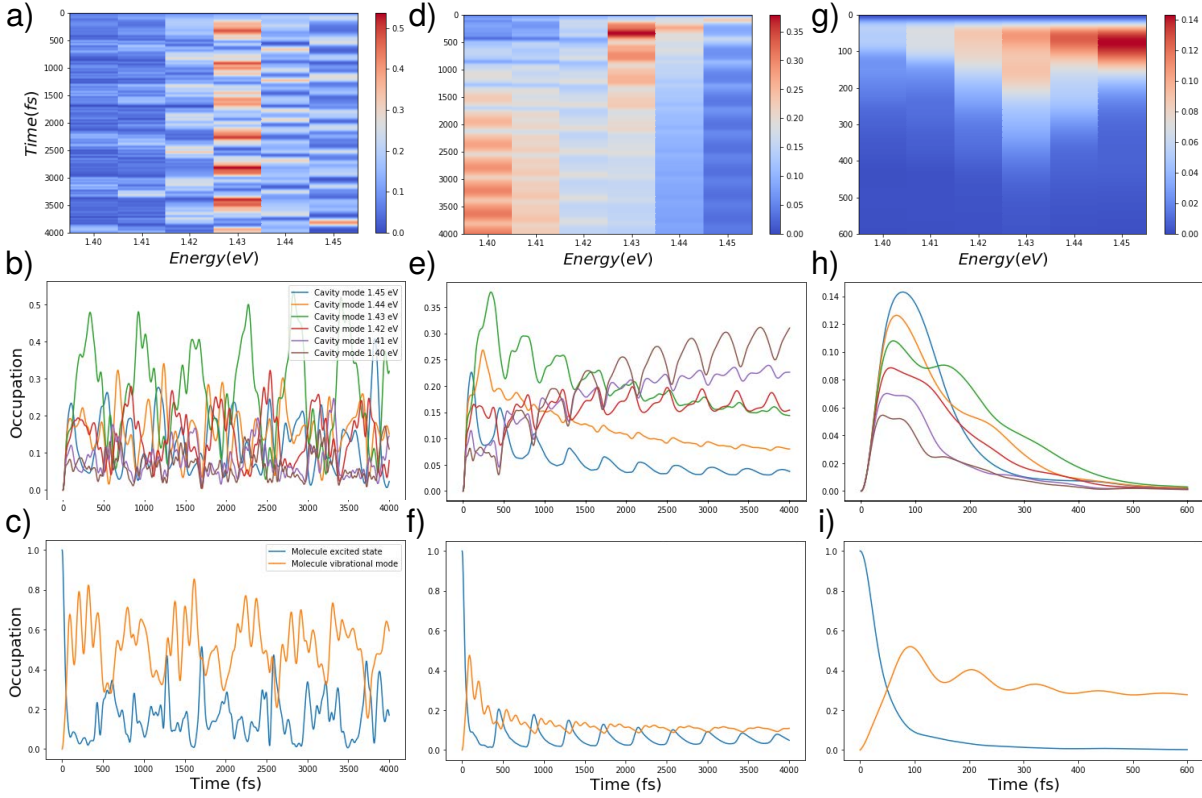


**Figure S7: Results of the quantum model.** Time evolution of the occupation probability of cavity modes and the molecule excited state and the vibrational mode. Results are shown for the cases of (a-c) no losses, (d-f) only the vibrational mode loss, and (g-i) all losses present. The parameters used in the simulation are listed in the Supplementary text. Here (a,d,g) show the occupations of cavity modes at different energies in a color scale, and (b,e,h) their time evolution. Molecule electronic excited state and vibrational state population time evolution is shown in (c,f,i). When there are no losses (a-c), the occupation oscillates reversibly between different cavity modes and the molecule excited state. Applying the vibrational mode dissipation (d-f) results in red shift of the occupation towards the lowest-energy cavity mode. (g-i) shows that even in the presence of losses, the occupation reaches a lower-energy cavity mode before vanishing. Note that the cavity mode at 1.43 eV (green solid line in (b,e,h)) is favoured because it resides at the energy  $\omega_m - \omega_v + \Delta$ , in other words, it corresponds to a resonance where original excited state energy of the molecule is distributed to a vibrational excitation and the cavity mode. Here  $\Delta$  is energy offset due to coupling between the molecule and the cavity modes. The shift can be approximated as  $\Delta \approx \sum_i |g|^2 / (\omega_m - \omega_i)$ .

## Section S10. Different pump pulse durations

We studied the condensation phenomenon as a function of pump pulse duration and found that thermalization and condensation happens only for sub-250 fs pump pulses. Comparison of 50 fs and 500 fs pump pulses is presented in Fig. S8. It is evident that the longer excitation pulse results in only one (lasing) threshold. The distributions at around the threshold (blue and red curves in Fig. S8a,e are similar with both pulse durations, but at the higher fluences (yellow, purple, and green curves) the distributions are very different. With a 500 fs pulse, the population does not reach a thermal Maxwell–Boltzmann distribution, and no narrow peaks appear at the band edge. Besides the luminescence intensity, the different threshold behaviour is clearly visible in the FWHM curves (Fig. S8c,g). The FWHM is significantly decreased with both pulse durations at the first (lasing) threshold but only in the 50-fs case, the FWHM is decreased even further at the second (condensation) threshold. Note that at intermediate pump fluences, the 50 fs pulse shows a sharp increase of the FWHM because the maximum of the line spectra is found at higher energies (see Fig. S8d) as the thermalizing population dominates the signal. Examples of real space and  $k$ -space images and spectra for the 500 fs are shown in Fig. S9, for pump fluences corresponding to the (a,c) lasing threshold and (b,d) beyond the condensation threshold of the 50 fs pump pulse. Importantly the real space and  $k$ -space images and spectra look nearly identical for both pump fluences for the 500 fs pulse duration, confirming that there indeed is no second threshold where the condensation would take place.

Fig. S10 presents the population distributions obtained from real space spectra for different pump pulse durations as well as the pump fluence dependence of the total luminescence intensity. The line spectra are shown for a pump fluence of  $3.5 \text{ mJ/cm}^2$  which is the same as for the condensation with 50 fs pump pulse in manuscript Fig. 2. There is a gradual evolution of the line spectra from thermalized distribution with a 100 fs pulse to a non-thermalized distribution and no narrow condensate peaks at the band edge with  $>250$  fs pulses. Notice that the actual mode line widths at the lasing regime cannot be extracted from the real space spectra as the lasing is spread along the TM mode that has a (relatively flat) parabolic dispersion. This means that the actual line widths in the  $k$ -space dispersions are smaller than what is observed in the real space spectra.

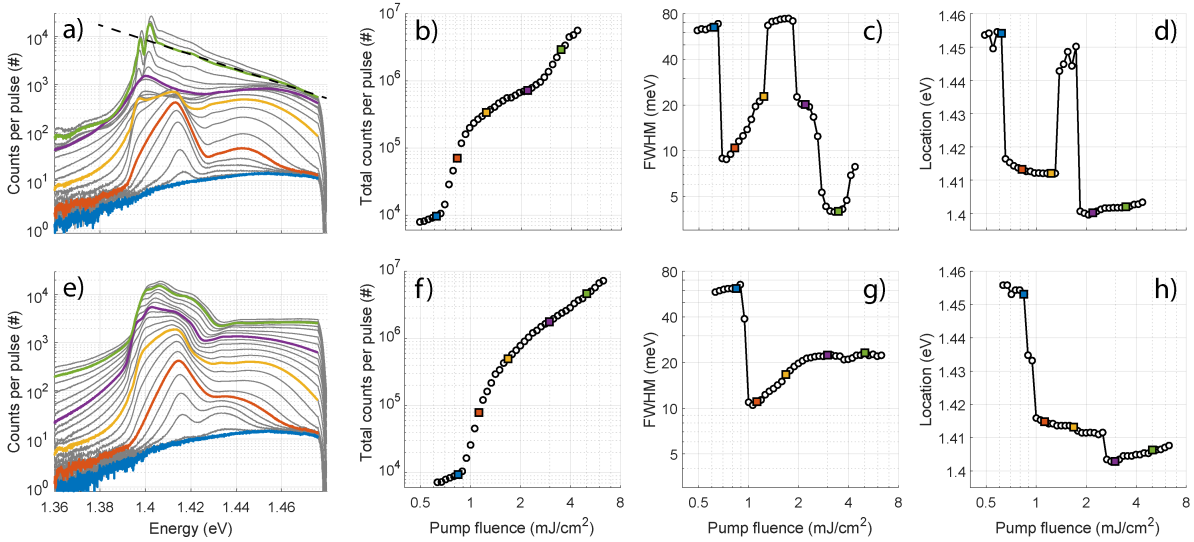


**Figure S8: Pump fluence dependence and line spectra for 50 fs and 500 fs pulse durations.** First column: Population distribution at different pump fluences. Second column: Fluence dependence of the total luminescence, summed counts under the curves in (a,e), showing the threshold behaviour. Third column: The full-width at half-maximum (FWHM) of the spectral maximum as a function of pump fluence. Fourth column: The energy position of the spectral maximum. The results are shown for two excitation pulse durations: (a-d) 50 fs and (e-h) 500 fs. The pump fluences indicated by colored markers in (b-d,f-h) correspond to the colored lines in (a,e). The short excitation pulse results in the double threshold behaviour with distinct regimes of lasing, incomplete thermalization, and condensation, as explained in the manuscript. Before the onset of the first threshold (blue), the distribution reflects the spontaneous emission profile of the molecule. When the first threshold is reached (red), lasing peak is visible at around the band edge energy. After the first threshold (yellow and purple), population at broad range of higher energies is increased due to incomplete thermalization (intermediate regime). Condensation takes place at the second threshold (green), only for the 50 fs pulse, where narrow peaks are observed at the band edge, followed by a thermalized tail at the higher energies. Fit to the Maxwell–Boltzmann distribution (dashed line in (a)) gives the temperature of  $333 \pm 12$  K.

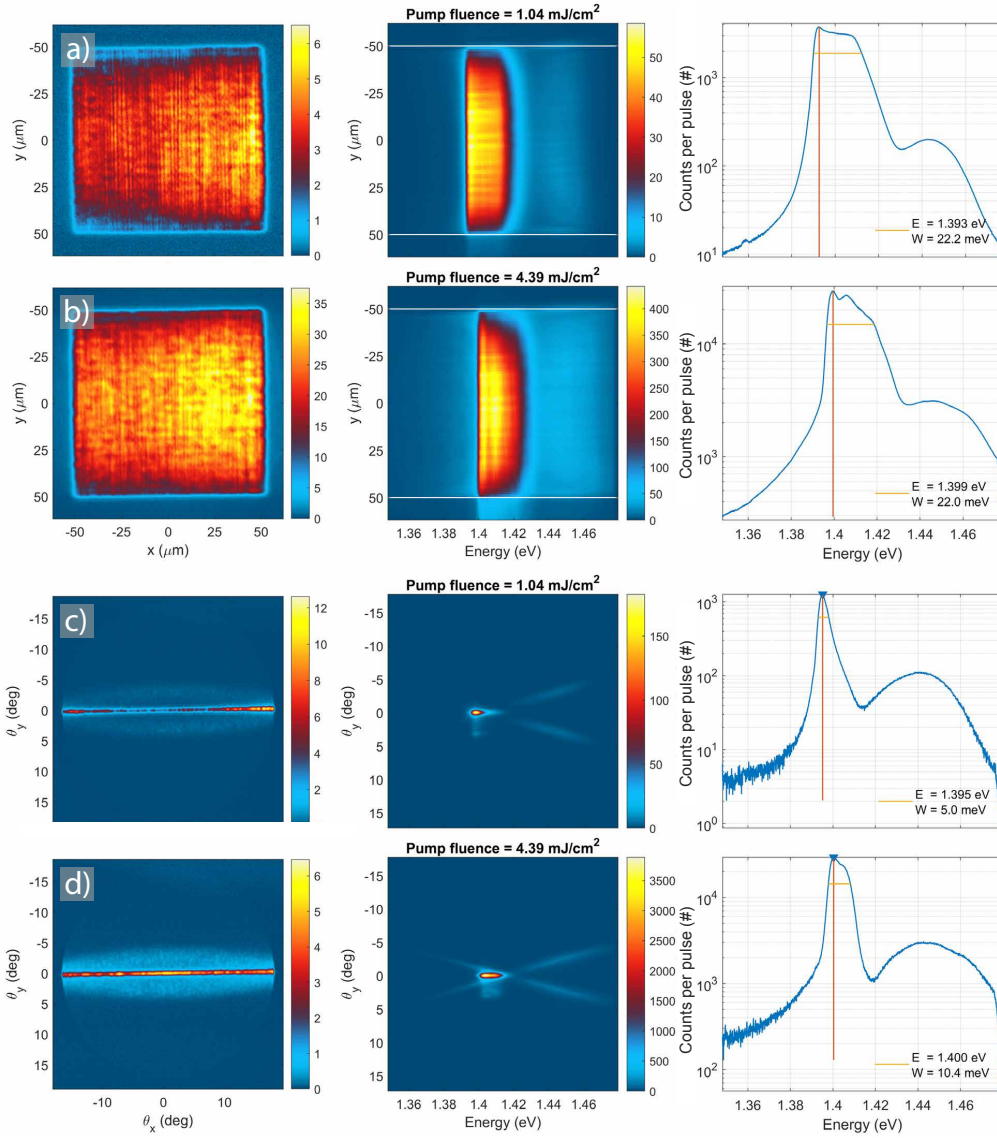


Figure S9: **Real space and  $k$ -space measurement with pump pulse duration of 500 fs.** (a-b) Real space measurements. Left column: Real space images. Middle column: Real space spectra. Right column: Line spectra of the intensity integrated over the real space spectra along  $y$ -axis between the white lines. (c-d)  $k$ -space measurements. Left column: 2D  $k$ -space images. Middle column:  $k$ -space spectra. Right column: Line spectra of the intensity integrated over the  $k$ -space spectra. The results are shown for a low (a,c) and a high (b,d) pump fluence. With a 500 fs pulse, we observe only the lasing regime where a narrow peak occurs at the band edge and some amplified spontaneous emission occurs in the dispersion branches, both above and below the crossing point. The luminescence from low to high pump fluences is spread widely in the TM mode, with little intensity seen at higher energies in the TE mode – no sign of thermalizing population nor 2D confinement.

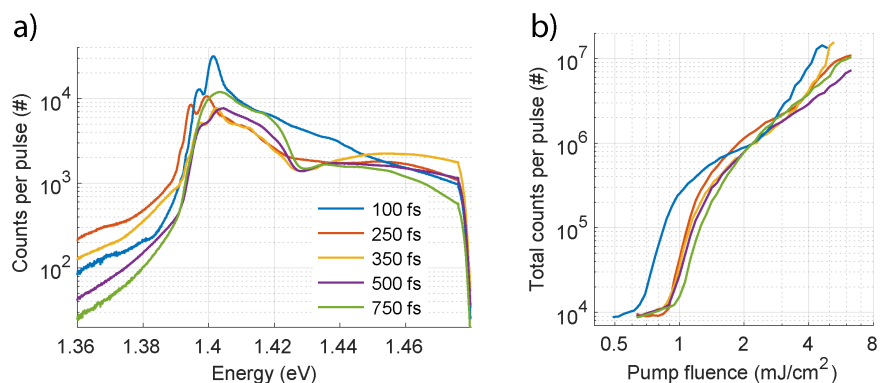


Figure S10: **Pump fluence dependence and line spectra for different pump pulse durations.** (a) Line spectra for different pulse durations at pump fluence of 3.5 mJ/cm<sup>2</sup>. Condensation occurs for the 100 fs pulse, but not for longer pulses. The spectrum for the 100 fs pulse duration (blue solid line) is similar to that measured with a 50 fs pulse presented in the manuscript: macroscopic population at the band edge followed by thermalized tail at the higher energies. (b) Total luminescence intensity as a function of pump fluence. Increasing the pump pulse duration increases slightly the first (lasing) threshold, whereas the second (condensation) threshold is clearly visible only for the 100 fs pulse.

## References

1. E. Altman, L. M. Sieberer, L. Chen, S. Diehl, and J. Toner, “Two-Dimensional Superfluidity of Exciton Polaritons Requires Strong Anisotropy,” *Physical Review X*, vol. 5, p. 011017, Feb. 2015.
2. J. Keeling, L. M. Sieberer, E. Altman, L. Chen, S. Diehl, and J. Toner, “Superfluidity and Phase Correlations of Driven Dissipative Condensates,” in *Universal Themes of Bose-Einstein Condensation*, pp. 205–230, Cambridge University Press, 2017. arXiv: 1601.04495.
3. D. Vorberg, W. Wustmann, R. Ketzmerick, and A. Eckardt, “Generalized Bose-Einstein Condensation into Multiple States in Driven-Dissipative Systems,” *Physical Review Letters*, vol. 111, p. 240405, Dec. 2013.
4. P. Kirton and J. Keeling, “Superradiant and lasing states in driven-dissipative Dicke models,” *New Journal of Physics*, vol. 20, p. 015009, Jan. 2018.
5. H. J. Hesten, R. A. Nyman, and F. Mintert, “Decondensation in Nonequilibrium Photonic Condensates: When Less Is More,” *Physical Review Letters*, vol. 120, p. 040601, Jan. 2018.
6. N. G. Berloff, M. Silva, K. Kalinin, A. Askitopoulos, J. D. Töpfer, P. Cilibrizzi, W. Langbein, and P. G. Lagoudakis, “Realizing the classical XY Hamiltonian in polariton simulators,” *Nature Materials*, vol. 16, pp. 1120–1126, Nov. 2017.
7. M. Heyl, “Dynamical quantum phase transitions: a review,” *Reports on Progress in Physics*, vol. 81, p. 054001, Apr. 2018.
8. I. Bloch, J. Dalibard, and W. Zwerger, “Many-body physics with ultracold gases,” *Reviews of Modern Physics*, vol. 80, pp. 885–964, July 2008.
9. P. Törmä and K. Sengstock, *Quantum Gas Experiments – Exploring Many-Body States*. Imperial College Press, 2015.

10. H. Deng, G. Weihs, C. Santori, J. Bloch, and Y. Yamamoto, “Condensation of Semiconductor Microcavity Exciton Polaritons,” *Science*, vol. 298, pp. 199–202, Oct. 2002.
11. J. Kasprzak, M. Richard, S. Kundermann, A. Baas, P. Jeambrun, J. M. J. Keeling, F. M. Marchetti, M. H. Szymańska, R. André, J. L. Staehli, V. Savona, P. B. Littlewood, B. Deveaud, and L. S. Dang, “Bose–Einstein condensation of exciton polaritons,” *Nature*, vol. 443, pp. 409–414, Sept. 2006.
12. R. Balili, V. Hartwell, D. Snoke, L. Pfeiffer, and K. West, “Bose-Einstein Condensation of Microcavity Polaritons in a Trap,” *Science*, vol. 316, pp. 1007–1010, May 2007.
13. J. J. Baumberg, A. V. Kavokin, S. Christopoulos, A. J. D. Grundy, R. Butté, G. Christmann, D. D. Solnyshkov, G. Malpuech, G. Baldassarri Höger von Högersthal, E. Feltin, J.-F. Carlin, and N. Grandjean, “Spontaneous Polarization Buildup in a Room-Temperature Polariton Laser,” *Physical Review Letters*, vol. 101, p. 136409, Sept. 2008.
14. S. Kéna-Cohen and S. R. Forrest, “Room-temperature polariton lasing in an organic single-crystal microcavity,” *Nature Photonics*, vol. 4, pp. 371–375, June 2010.
15. I. Carusotto and C. Ciuti, “Quantum fluids of light,” *Reviews of Modern Physics*, vol. 85, pp. 299–366, Feb. 2013.
16. T. Byrnes, N. Y. Kim, and Y. Yamamoto, “Exciton-polariton condensates,” *Nature Physics*, vol. 10, pp. 803–813, Nov. 2014.
17. K. S. Daskalakis, S. A. Maier, R. Murray, and S. Kéna-Cohen, “Nonlinear interactions in an organic polariton condensate,” *Nature Materials*, vol. 13, pp. 271–278, Mar. 2014.
18. J. D. Plumhof, T. Stöferle, L. Mai, U. Scherf, and R. F. Mahrt, “Room-temperature Bose–Einstein condensation of cavity exciton–polaritons in a polymer,” *Nature Materials*, vol. 13, pp. 247–252, Mar. 2014.
19. J. Klaers, J. Schmitt, F. Vewinger, and M. Weitz, “Bose-Einstein condensation of photons in an optical microcavity,” *Nature*, vol. 468, pp. 545–548, Nov. 2010.

20. J. Schmitt, “Dynamics and correlations of a Bose–Einstein condensate of photons,” *Journal of Physics B: Atomic, Molecular and Optical Physics*, vol. 51, p. 173001, Aug. 2018.
21. J. Schmitt, T. Damm, D. Dung, F. Vewinger, J. Klaers, and M. Weitz, “Observation of Grand-Canonical Number Statistics in a Photon Bose-Einstein Condensate,” *Physical Review Letters*, vol. 112, p. 030401, Jan. 2014.
22. R. Weill, A. Bekker, B. Levit, and B. Fischer, “Bose-Einstein condensation of photons in an erbium-ytterbium co-doped fiber cavity,” *Nature Communications*, vol. 10, p. 747, Feb. 2019.
23. W. Wang, M. Ramezani, A. I. Väkeväinen, P. Törmä, J. G. Rivas, and T. W. Odom, “The rich photonic world of plasmonic nanoparticle arrays,” *Materials Today*, vol. 21, pp. 303–314, Apr. 2018.
24. W. Zhou, M. Dridi, J. Y. Suh, C. H. Kim, D. T. Co, M. R. Wasielewski, G. C. Schatz, and T. W. Odom, “Lasing action in strongly coupled plasmonic nanocavity arrays,” *Nature Nanotechnology*, vol. 8, pp. 506–511, July 2013.
25. A. H. Schokker and A. F. Koenderink, “Lasing at the band edges of plasmonic lattices,” *Physical Review B*, vol. 90, p. 155452, Oct. 2014.
26. A. Yang, T. B. Hoang, M. Dridi, C. Deeb, M. H. Mikkelsen, G. C. Schatz, and T. W. Odom, “Real-time tunable lasing from plasmonic nanocavity arrays,” *Nature Communications*, vol. 6, p. 6939, Apr. 2015.
27. T. K. Hakala, H. T. Rekola, A. I. Väkeväinen, J.-P. Martikainen, M. Nečada, A. J. Moilanen, and P. Törmä, “Lasing in dark and bright modes of a finite-sized plasmonic lattice,” *Nature Communications*, vol. 8, p. 13687, Jan. 2017.
28. T. K. Hakala, A. J. Moilanen, A. I. Väkeväinen, R. Guo, J.-P. Martikainen, K. S. Daskalakis, H. T. Rekola, A. Julku, and P. Törmä, “Bose-Einstein condensation in a plasmonic lattice,” *Nature Physics*, vol. 14, p. 739, July 2018.

29. M. Ramezani, A. Halpin, A. I. Fernández-Domínguez, J. Feist, S. R.-K. Rodriguez, F. J. Garcia-Vidal, and J. G. Rivas, “Plasmon-exciton-polariton lasing,” *Optica*, vol. 4, pp. 31–37, Jan. 2017.
30. M. De Giorgi, M. Ramezani, F. Todisco, A. Halpin, D. Caputo, A. Fieramosca, J. Gomez-Rivas, and D. Sanvitto, “Interaction and Coherence of a Plasmon–Exciton Polariton Condensate,” *ACS Photonics*, vol. 5, pp. 3666–3672, Aug. 2018.
31. D. Bajoni, P. Senellart, A. Lemaître, and J. Bloch, “Photon lasing in  $\mathrm{GaAs}$  microcavity: Similarities with a polariton condensate,” *Physical Review B*, vol. 76, p. 201305, Nov. 2007.
32. J. Schmitt, T. Damm, D. Dung, F. Vewinger, J. Klaers, and M. Weitz, “Thermalization kinetics of light: From laser dynamics to equilibrium condensation of photons,” *Physical Review A*, vol. 92, p. 011602, July 2015.
33. B. T. Walker, L. C. Flatten, H. J. Hesten, F. Mintert, D. Hunger, A. A. P. Trichet, J. M. Smith, and R. A. Nyman, “Driven-dissipative non-equilibrium Bose–Einstein condensation of less than ten photons,” *Nature Physics*, vol. 14, p. 1173, Dec. 2018.
34. V. G. Kravets, A. V. Kabashin, W. L. Barnes, and A. N. Grigorenko, “Plasmonic Surface Lattice Resonances: A Review of Properties and Applications,” *Chemical Reviews*, vol. 118, pp. 5912–5951, June 2018.
35. P. Törmä and W. L. Barnes, “Strong coupling between surface plasmon polaritons and emitters: a review,” *Reports on Progress in Physics*, vol. 78, no. 1, p. 013901, 2015.
36. K. S. Daskalakis, A. I. Väkeväinen, J.-P. Martikainen, T. K. Hakala, and P. Törmä, “Ultrafast Pulse Generation in an Organic Nanoparticle-Array Laser,” *Nano Letters*, vol. 18, pp. 2658–2665, Apr. 2018.
37. A. E. Siegman, *Lasers*. Mill Valley, CA: University Science Books, 1986.
38. P. Kirton and J. Keeling, “Nonequilibrium Model of Photon Condensation,” *Physical Review Letters*, vol. 111, p. 100404, Sept. 2013.

39. A. Chiocchetta, A. Gambassi, and I. Carusotto, “Laser Operation and Bose-Einstein Condensation: Analogies and Differences,” in *Universal Themes of Bose-Einstein Condensation*, pp. 409–423, Cambridge University Press, 2017.
40. N. Somaschi, L. Mouchliadis, D. Coles, I. E. Perakis, D. G. Lidzey, P. G. Lagoudakis, and P. G. Savvidis, “Ultrafast polariton population build-up mediated by molecular phonons in organic microcavities,” *Applied Physics Letters*, vol. 99, p. 143303, Oct. 2011.
41. K. Yamashita, U. Huynh, J. Richter, L. Eyre, F. Deschler, A. Rao, K. Goto, T. Nishimura, T. Yamao, S. Hotta, H. Yanagi, M. Nakayama, and R. H. Friend, “Ultrafast Dynamics of Polariton Cooling and Renormalization in an Organic Single-Crystal Microcavity under Nonresonant Pumping,” *ACS Photonics*, vol. 5, pp. 2182–2188, June 2018.
42. F. Herrera and F. C. Spano, “Theory of Nanoscale Organic Cavities: The Essential Role of Vibration-Photon Dressed States,” *ACS Photonics*, vol. 5, pp. 65–79, Jan. 2018.
43. A. Strashko, P. Kirton, and J. Keeling, “Organic Polariton Lasing and the Weak to Strong Coupling Crossover,” *Physical Review Letters*, vol. 121, p. 193601, Nov. 2018.
44. J. del Pino, F. A. Schröder, A. W. Chin, J. Feist, and F. J. Garcia-Vidal, “Tensor Network Simulation of Non-Markovian Dynamics in Organic Polaritons,” *Physical Review Letters*, vol. 121, p. 227401, Nov. 2018.
45. N. Shammah, S. Ahmed, N. Lambert, S. De Liberato, and F. Nori, “Open quantum systems with local and collective incoherent processes: Efficient numerical simulations using permutational invariance,” *Physical Review A*, vol. 98, p. 063815, Dec. 2018.
46. P. Kirton, M. M. Roses, J. Keeling, and E. G. D. Torre, “Introduction to the Dicke Model: From Equilibrium to Nonequilibrium, and Vice Versa,” *Advanced Quantum Technologies*, vol. 2, no. 1-2, p. 1800043, 2019.
47. R. F. Ribeiro, L. A. Martínez-Martínez, M. Du, J. Campos-Gonzalez-Angulo, and J. Yuen-Zhou, “Polariton chemistry: controlling molecular dynamics with optical cavities,” *Chemical Science*, vol. 9, no. 30, pp. 6325–6339, 2018.

48. M. Hertzog, M. Wang, J. Mony, and K. Börjesson, “Strong light–matter interactions: a new direction within chemistry,” *Chemical Society Reviews*, vol. 48, no. 3, pp. 937–961, 2019.
49. D. Wang, A. Yang, W. Wang, Y. Hua, R. D. Schaller, G. C. Schatz, and T. W. Odom, “Band-edge engineering for controlled multi-modal nanolasing in plasmonic superlattices,” *Nature Nanotechnology*, vol. 12, pp. 889–894, Sept. 2017.
50. G. Mie, “Beiträge Zur Optik Trüber Medien, Speziell Kolloidaler Metallösungen,” *Ann. Phys.*, vol. 330, pp. 377–445, Jan. 1908.
51. Y.-I. Xu, “Efficient Evaluation of Vector Translation Coefficients in Multiparticle Light-Scattering Theories,” *Journal of Computational Physics*, vol. 139, pp. 137–165, Jan. 1998.
52. R. Guo, M. Nečada, T. K. Hakala, A. I. Väkeväinen, and P. Törmä, “Lasing at  $K$  Points of a Honeycomb Plasmonic Lattice,” *Phys. Rev. Lett.*, vol. 122, p. 013901, Jan. 2019.
53. M. Tavis and F. W. Cummings, “Exact Solution for an  $N$ -Molecule—Radiation-Field Hamiltonian,” *Physical Review*, vol. 170, pp. 379–384, June 1968.
54. J. A. Ćwik, S. Reja, P. B. Littlewood, and J. Keeling, “Polariton condensation with saturable molecules dressed by vibrational modes,” *EPL (Europhysics Letters)*, vol. 105, p. 47009, Feb. 2014.
55. F. Herrera and F. C. Spano, “Cavity-Controlled Chemistry in Molecular Ensembles,” *Physical Review Letters*, vol. 116, p. 238301, June 2016.
56. N. Wu, J. Feist, and F. J. Garcia-Vidal, “When polarons meet polaritons: Exciton-vibration interactions in organic molecules strongly coupled to confined light fields,” *Physical Review B*, vol. 94, p. 195409, Nov. 2016.
57. H.-P. Breuer and F. Petruccione, *The Theory of Open Quantum Systems*. Oxford University Press, 2002.
58. J. R. Johansson, P. D. Nation, and F. Nori, “QuTiP: An open-source Python framework for the dynamics of open quantum systems,” *Computer Physics Communications*, vol. 183, pp. 1760–1772, Aug. 2012.